

1 **A 3000-year Record of Surface Rupturing Earthquakes at Gunalan;**
2 **Variable Fault Rupture Lengths on the 1939 Erzincan Earthquake**
3 **Rupture Segment of the North Anatolian Fault, Turkey**

4 Short title: Paleoseismology Gunalan Turkey

5 AUTHORS:

6 **Fraser, J. G.*¹**, Hubert-Ferrari, A.¹, Verbeeck, K.¹, Garcia-Moreno, D.¹, Avsar, U.¹,
7 Maricq, N.², Coudijzer, A.³, Vlamynck, N.³ Vanneste, K.¹

8 *Corresponding author is Dr. Jeff Fraser (jeph4e@gmail.com, Ph: 00447523567585, no fax)

9 1 Royal Observatory of Belgium
10 Seismology Section
11 Avenue Circulaire 3
12 1180 Brussels
13 Belgium

14 2 Université Libre de Bruxelles
15 Département des Sciences de la Terre et de L'Environnement
16 Avenue F.D. Roosevelt 50
17 B-1050 Brussels
18 Belgium

19 3 University of Gent
20 Department of Geology and Soil Science
21 Krijgslaan 281
22 9000 Gent
23 Belgium

24

Aurelia.Ferrari@ulg.ac.be	nathaliemaricq@gmail.com
koen.verbeeck@oma.be	alexander.coudijzer@gmail.com
davidgm08@gmail.com	neel_le@hotmail.com
avsarulas@yahoo.com	kris.vanneste@oma.be

25 Key words: Paleoseismology, North Anatolian Fault

26 04.04.01. Earthquake geology and paleoseismology

27 04.06.01. Earthquake faults: properties and evolution

28 04.07.04. Plate boundaries, motion, and tectonics

29

30 **Abstract**

31 The North Anatolian Fault is a ~1200 km long right-lateral strike-slip fault that forms the
32 northern boundary of the Anatolian plate. A damaging sequence of earthquakes ruptured
33 almost the entire fault in the twentieth century. This study adds to the growing number of
34 paleoseismic investigations on the 350 km long 1939 Erzincan earthquake rupture
35 segment, which is toward the eastern end of the North Anatolian Fault in Turkey. Using
36 three paleoseismic trenches located along about 2km of the principal fault strand, this
37 study determines the timing of five earthquakes prior to the 1939 earthquake. The first
38 three earthquakes are correlated to historical earthquakes in A.D. 1668, 1254, 499 and
39 two further events were identified at 881 – 673 B.C. and 1406 – 1291 B.C. (2σ age
40 ranges). By comparing the earthquake timing determined in this study to the results of
41 other paleoseismic investigations on the 1939 rupture segment, it becomes clear that this
42 historical rupture segment does not always rupture in unison. This analysis indicates that
43 the A.D. 499 earthquake was the last time the 1939 rupture segment ruptured in unison;
44 although partial ruptures of the 1939 rupture segment occur more frequently and also
45 produce large magnitude earthquakes ($> M_w 7$).

46

47 **1. Introduction**

48 The Anatolian plate is moving toward the west, principally due to the collision of the
49 Arabian plate into Eurasia (Fig. 1a, e.g. *Flerit et al.*, 2004; *Sengor et al.*, 2005). During
50 the twentieth century a sequence of large magnitude earthquakes ruptured most of the
51 NAF causing catastrophe to local populations and infrastructure (e.g. *Barka*, 1996). This
52 sequence of large earthquakes began with the 1939 Erzincan earthquake and proceeded to
53 migrate in a cascading sequence, first to the west and then to the east and west (*Stein et*
54 *al.*, 1997). The most recent large surface-rupturing earthquakes in the sequence occurred
55 near the eastern end of the Marmara Sea in 1999 (i.e. *Barka et al.*, 2002; *Gulen et al.*,
56 2002). *Stein et al.* (1997) modeled the Coulomb failure stress changes caused by the
57 earthquakes of the twentieth-century earthquake sequence on the NAF. They found that
58 earthquake-induced stress changes raised the probability of fault rupture at the sites
59 where subsequent earthquakes occurred (*Stein et al.*,1997). Fault rupture causes a stress
60 drop on the slipped fault and an increases in stress at nearby locations, hence bringing
61 nearby faults closer to failure (*Stein et al.*,1997). Where nearby faults have already
62 accumulated near-critical stress levels this can trigger an earthquake. This process
63 suggests a mechanism for the cascading twentieth-century sequence of large earthquake
64 on the NAF. However, it does require that the levels of stress along the sections of the
65 fault that ruptured in the twentieth century sequence were all at a near-critical level. This
66 raises the question; does the NAF always rupture in a cascading sequence like that
67 observed in the twentieth century?

68 Turkey has a long historical record of earthquakes (e.g. *Ambraseys*, 1970; *Ambraseys and*
69 *Finkel*, 1995; *Ambraseys and Jackson*, 1998; *Guidoboni and Comastri*, 2005; *Guidoboni*
70 *et al.*, 1994; *Nur and Cline*, 2000; *Sengor et al.*, 2005). We have compiled a list of
71 historical earthquakes that may have ruptured all or part of the 1939 Erzincan fault
72 rupture segment from various sources (Table. 1). Historical earthquake records are
73 typically temporally precise and accurate compared to the results of paleoseismic
74 investigations which have relatively low precision in time because of the uncertainties
75 inherent in constraining paleoearthquake ages. However, historical earthquake records
76 are typically spatially imprecise (i.e. it is seldom specified which fault or fault segment(s)

77 ruptured to cause an earthquake) whereas paleoseismic investigations can yield
78 earthquake records for a specific point on a particular fault strand. A paleoseismic trench
79 investigation can constrain when a particular fault strand ruptured the ground surface; by
80 using radiocarbon dating in conjunction with Bayesian statistical modeling (*Biasi and*
81 *Weldon, 1994; Biasi et al., 2002; Hilley and Young, 2008a, 2008b*) we can obtain
82 relatively precise paleoearthquake timing that incorporates quantification of uncertainty.
83 By comparing paleoearthquake timing from paleoseismic trenching investigations at
84 multiple sites along adjoining fault segments, we can estimate the ground surface
85 rupturing length for large magnitude earthquakes (generally $M > 6.5$), which is a proxy
86 for paleoearthquake magnitude (e.g. *Wells and Coppersmith, 1994; Anderson et al.,*
87 *1999*). The completeness of earthquake records from both the historical and paleoseismic
88 investigations is uncertain because the absence of evidence is not evidence of absence
89 (i.e. neither means of investigation provides a definitive complete record of surface
90 rupturing earthquakes). Therefore combining the historical and paleoseismic data
91 provides the best long-term spatiotemporal earthquake data.

92 To date, more than 50 paleoseismic investigations have been conducted along the NAF.
93 In the present study, we focus on the 1939 Erzincan Earthquake rupture segment. There
94 have been many paleoseismic investigations along this segment, particularly in the area
95 immediately west of this study area, however these results have not been published (i.e.
96 conference abstracts: *Okumura et al., 1994; Zabcı et al., 2008*) but investigations at
97 Resadiye (*Fraser, 2009b*), Yaylabeli (*Kozacı et al., 2011*) and Cukurcimen (*Hartleb et*
98 *al., 2006*) are publicly available.

99 This paper presents a paleoseismic study at Gunalan (N:40.024°, E:38.627°), which is
100 located on the 1939 Erzincan earthquake rupture segment (Fig. 1b). The magnitude M_w
101 7.7 (*Anderson et al., 1996*) Erzincan earthquake caused widespread damage and loss of
102 life (*Barka, 1996*). The paleoseismic investigation at Gunalan focuses on determining a
103 long record of the timing of paleoearthquakes. The paleoearthquake chronology
104 determined in this study has been used by *Fraser et al. (2010a)*, who summarize publicly
105 available paleoearthquake data on the NAF and compare the data from selected studies

106 along the entire NAF. Gunalan is located between previous paleoseismic investigations
107 on the 1939 Erzincan earthquake rupture segment at Resadiye (*Fraser, 2009b*) to the west
108 and Yaylabeli (*Kozaci et al., 2011*) and Cukurcimen (*Hartleb et al., 2006*) to the east
109 (Fig. 1b). In this paper the timing of paleoearthquakes determined at Gunalan is
110 compared with the timing of paleoearthquakes determined in the other paleoseismic
111 investigations on the 1939 Erzincan Earthquake fault rupture segment and with the
112 historical earthquake record (Table 1), to investigate the nature of fault rupture along this
113 section of the fault during the preceding cycles of seismicity.

114 **2. Regional Tectonic Setting**

115 Over geological time, as the Arabian plate moves northward relative to the Eurasian
116 plate, the wedge-shaped Anatolian plate is squeezed in an approximately north-south
117 direction causing it to translate toward the west (Fig.1a). Back-arc extension in the
118 Aegean region, associated with subduction at the Hellenic arc, may provide a pulling
119 force on the Anatolian Plate (*Flerit et al., 2004; Pondard et al., 2007*). The North
120 Anatolian Fault (NAF) formed in a similar tectonic regime as the present and initiated in
121 the east around 13 Ma (*Sengor et al., 1985*). Utilizing weaknesses in the lithosphere
122 associated with pre-existing suture zones the proto-NAF propagated westwards, reaching
123 the Marmara Sea by about 5 Ma (*Armijo et al., 1999; Hubert-Ferrari et al., 2002*)
124 although this is still debated (e.g. *Sengor et al., 2005*). Offset features such as suture
125 zones, prominent geomorphic features, the Niksar and Tasova-Erbaa pull-apart basins,
126 and other basins that developed during the formation of the NAF, suggest that it has
127 undergone a total of approximately 85 km of right-lateral offset (e.g. *Barka et al., 2000;*
128 *Hubert-Ferrari et al., 2009; Sengor et al., 2005*).

129 Offset Holocene geomorphic features along the NAF suggest a slip-rate of 18.5 ± 3.5
130 mm/yr with a right-lateral strike-slip style (*Hubert-Ferrari et al., 2002*). A GPS based
131 study of the Eastern Mediterranean region (*Reilinger et al., 2006*) indicates that the rate
132 of right-lateral strike-slip offset in the vicinity of the study area is approximately
133 27.7 ± 0.2 mm/yr with a negligible extensional component. Thus, the Holocene slip rate is

134 ~65% of the GPS-based slip rate. However, because the GPS data have only been
135 collected after the twentieth-century earthquake sequence it may also account for some
136 post-seismic relaxation. Furthermore, because GPS monitoring stations are mostly
137 located a significant distance from the NAF, GPS rates also account for deformation on
138 subordinate plate boundary structures (faults and folds) and intra-plate deformation. The
139 comparison of GPS-based and Holocene geomorphic deformation based slip rates
140 suggests that most of the tectonic deformation associated with the northern edge of the
141 Anatolian plate is accommodated by the NAF, with considerably less than 35% of the
142 tectonic deformation accommodated intra-plate.

143 The East Anatolian Fault (EAF) accommodates the left-lateral strike-slip deformation on
144 the Anatolian-Arabian plate boundary, which is the southeastern margin of the Anatolian
145 plate. Other individual faults near the plate boundary and within the Anatolian plate are
146 likely to be significantly less active (perhaps accommodating an order of magnitude less
147 deformation). For example, the Ovacik (OF) and Almus Faults (AlF) (Fig. 1b)
148 accommodate some of the Anatolian-Eurasian plate boundary deformation within the
149 Anatolian plate. Some of the Eurasian-Anatolian plate boundary movement is
150 accommodated by faults to the north of the NAF; for example the North East Anatolian
151 Fault (NEAF) (Fig1b). Notably, the geological history and activity of many of these
152 faults, particularly those located away from the principal plate boundary faults, are not
153 well constrained. Therefore, it is only possible to speculate about the relationships
154 concerning crustal stress and strain between these faults and the NAF.

155 *2.1. Neotectonics near the study area*

156 Our study area is located near the western end of the Mihar-Tumekar fault segment
157 (*Barka*, 1996, Fig. 1) on the southern side of the Golova basin. Kocyigit (1990)
158 described the Golova basin as an active basin along this segment of the NAF and
159 Kocyigit (1989) described the Susehri basin, which is located immediately west of the
160 Golova basin, as an active fault wedge basin. We speculate that the Golova and Susehri
161 basins were originally one pull-apart basin that was abandoned in favor of a new
162 optimally oriented principal deformation zone through the pull-apart basin. This

163 abandonment of the proto Susehri-Golova pull-apart basin may be coincident with the
164 abandonment of the Tasova-Erbaa pull-apart basin ~125 km to the west (Fig. 1b)
165 documented by Barka *et al.* (2000). However, a detailed neotectonic study is required to
166 support this hypothesis. The presence of these neotectonic structures may have an
167 influence on fault rupture propagation on the Mihar-Tumekar and adjacent fault
168 segments.

169 **2.2. Fault Segmentation**

170 Active fault traces are generally not continuous, and have discontinuities that appear as
171 steps or bends in the fault geometry. Depending on their scale, such discontinuities may
172 slow or stop fault rupture propagation (Wesnousky, 2006). On strike-slip faults, map-
173 view steps in the fault trace cause transpressional or transtensional stress and strain,
174 resulting in structures such as pop-up structures and pull-apart basin, respectively.
175 Wesnousky (2006) studied the importance of the size of discontinuities for fault rupture
176 propagation using historical earthquakes on strike-slip faults and found that
177 discontinuities with step-over distances of up to 4 km could be ruptured across in an
178 individual event, although sometimes smaller discontinuities could inhibit fault rupture
179 propagation.

180 ‘Fault rupture segments’ are sections of a fault that have ruptured during one earthquake.
181 Thus, to define one, the extent of ground surface rupture must be mapped either soon
182 after an earthquake or by detailed observations of relict geological and/or
183 geomorphological features caused by ancient surface rupture (e.g. multiple paleoseismic
184 studies along a fault).

185 ‘Fault segments’ are sections of a fault bounded by discontinuities which may stop or
186 slow fault rupture propagation and a defined based on judgment of fault geometry.

187 The 1939 Erzincan earthquake fault rupture segment was described by Barka (1996) and
188 references therein; it extended from the Erzincan pull-apart basin in the east to near the
189 village of Ezinepazari in the west (Fig. 1b) with a rupture length of ~350 km (*Anderson et*

190 *al.* 1999). The western end of the rupture included the Ezinepazari fault which splays to
191 the southwest from the main NAF trace at the southern side of the Niksar pull-apart
192 basin.

193 Barka (1996) partitioned the 1939 Erzincan fault rupture segment in to five fault
194 segments as illustrated in Figure 1b and 1c. He defined the segment boundaries by
195 discontinuities in map view geometry of the active fault trace. Ezinepazari and Kelkit
196 Valley segments intersect at the south side of the Niksar pull-apart basin, the western and
197 eastern ends of the Ortakoy-Susehri segment are defined by significant bends in the fault
198 trace, and the Mihar-Tumekar to Erzincan fault segment boundary is defined as a 20°
199 restraining bend (see *Barka*, 1996 for further detail).

200 One aspect of this study is to investigate if the fault segments that ruptured in the 1939
201 Erzincan Earthquake always rupture in tandem by comparing the timing of
202 paleoearthquakes identified at Gunalan and three other locations along the fault rupture
203 segment.

204 **3. Tectonogeomorphology of the study area**

205 In this study we use tectonic geomorphology to identify the principal fault across which
206 to undertake paleoseismic trenching studies to investigate the timing of paleoearthquakes.
207 No tectonogeomorphic measurements have been made in this study. The study area is
208 located on the southeast side of the Cobanlı River, near the village of Gunalan
209 (N:40.024°, E:38.627°), on the southern side of the Golova basin (Fig. 1b). There are
210 three clearly active fault strands in the study area (Fig. 2a), which we have labeled Faults
211 A – C, from north to south (Fig. 2).

212 Locally, Kocuyigit (1990) documented a broad (~12km fault-normal) damage zone caused
213 by the 1939 earthquake with small vertical displacements on many faults, but the
214 majority of the slip (right-lateral) was accommodated by the principal deformation zone
215 fault (equivalent to Fault A in this study). This broad damage zone may reflect
216 reactivation of structures associated with the Golova basin.

217 Kocyigit (1990) measured four right-laterally offset features near the study area on the
218 principal deformation zone fault (Fault A), although we were unable to identify these
219 features during field work. The three right-lateral offsets were accompanied by 0.3m to
220 3.5m of vertical displacement and comprised: (1) a field boundary offset by 5.5m ~18km
221 west of Gunalan, (2) a field boundary offset by 6.4m ~13km west of Gunalan, (3) a line
222 of Poplar trees offset by 5.7m ~5km west of Gunalan, and (4) an irrigation canal offset by
223 5.6m ~2.5km (Fig. 2a) west of Gunalan (Kocyigit, 1990, pg 165). Right-lateral offset (4)
224 was used by Barka (1996) and is shown in Figure 1c. Additionally, Kocyigit (1990, pg
225 165) noted three locations where “...the southern and northern blocks alternately
226 subsided and uplifted up to 3.5m” and these were located: (5) ~300m east of Gunalan
227 (Fig. 2a), (6) ~600m northeast of Gunalan (Fig. 2a), and (7) ~14km east of Gunalan.
228 Kocyigit (1990) described a splay of the principal deformation zone fault that traces
229 along the northern side of a prominent elongate linear ridge shown in the middle of
230 Figures 2c and 2e on which offset (6) was attributed to the 1939 earthquake. We
231 recognized a lateral spread in this area (Fig. 2c and f) but no evidence of faulting. Lateral
232 spreads are a type of shallow translational landslide that occur on gently sloping to flat
233 ground and are relatively abundant during earthquakes due to failure on zones of
234 liquefied soils (Keefer, 1984). Discussions with local residents indicate that this lateral
235 spread occurred, or was at least reactivated, during the 1939 Erzincan Earthquake. We
236 interpret that this offset was actually attributable to the lateral spread. Kocyigit (1990, pg
237 165) also notes that the southern strand (fault C) of the bifurcated Coblani fault (faults B
238 and C) were “reactivated by ground ruptures” during the 1939 earthquake (see label 8 in
239 Figure 2a). Based on the geomorphological expression of the three fault strands in the
240 study area we are inclined to agree with Kocyigit’s (1990) interpretation of the relative
241 activity of fault strand A, B and C. The very clear tectonogeomorphic features associated
242 with fault A suggest that this is the principal deformation zone. Fault C has clear
243 geomorphic expression suggesting that this strand ruptured in the 1939 earthquake, while
244 Fault B has a less clear geomorphic expression suggesting that this strand did not rupture
245 in the 1939 earthquake.

246 The features of the study area are described from west to east (Fig. 2). The Cobanlı River
247 flows towards the north until it crosses the NAF, downstream of which it bends and flows
248 towards the east (Fig. 2a). The geomorphology of the western portion of the study area is
249 an alluvial flood plain across which fault A is evidenced by a subtle fault scarp (i.e. less
250 than ~0.2m) that steps down to the south. The ground is considerably wetter on the south
251 side of the fault, which corresponds to a recognizable change in vegetation color (Fig.
252 2b). Southeast of the alluvial plain the terrain is hilly, dominated by linear ridges that run
253 sub-parallel to the fault. We attribute these linear ridges to low-activity (relative to fault
254 A), possibly reactivated, fault strands. Local ephemeral streams, which generally flow
255 towards the north, have eroded gullies through the linear ridges at some locations. The
256 village of Gunalan is situated near the point where the trace of Fault A leaves the alluvial
257 plain to the west and passes into the hilly terrain (Fig. 2a) where it runs along the
258 southern side of an elongate linear ridge for approximately 3 km east of Gunalan.
259 Alluvial fan and wetland deposits fill a depression formed between the hills to the south
260 and the elongate linear ridge.

261 The elongate linear ridge is composed of Pliocene continental clastics of the Cobanlı
262 Group that is part of the Upper Pontus Formation (*Barka, 1992*). There are three possible
263 scenarios that may have formed the elongate linear ridge feature (in order of preference):

264 (1) Strike-slip offset Pliocene deposits making this primarily a shutter ridge. For this
265 scenario there is no need to have a bounding fault on the northern side of the
266 ridge, river erosion alone can explain the concaved slope break along the
267 northern side of the elongate linear ridge. This is consistent with our
268 interpretation that the fault mapped by Kocyigit (1990) on the northern side of
269 the elongate linear ridge is not present.

270 (2) A pop-up-structure or pressure ridge. For such a feature to form, there would
271 need to be a fault on the northern side of the elongate linear ridge, for which we
272 did not recognise any geomorphological evidence.

273 (3) A significant dip-slip component of displacement, down on the south side of the
274 fault, may have caused the topographic step on the south side of the ridge. The

275 topographic step down to the north on the northern side of the ridge may have
276 been caused by river bank erosion. Thus the elongate ridge would be the
277 remains of an elevated area comprising the hanging-wall block, the northern part
278 having been eroded away by the Cobanlı River.

279 While we cannot rule out any of these three scenarios, we think that scenario 1 is the
280 most probable as it is the simplest explanation. Regardless of how the elongate ridge
281 formed, it is clearly bounded by a fault on its southern side and the concave slope-break
282 at its base traps small alluvial fans from local northward draining ephemeral streams.
283 The fans have a typical conical geometry with apices at small valleys that drain the hills
284 to the south. Between the alluvial fans, where they abut the fault scarp, reed beds and
285 associated organic-rich wetland deposits have developed.

286 South of the elongate linear ridge faults B and C splay southward. Our interpretation of
287 the local geomorphology is that the depression between faults A and B (which the
288 alluvial fans are filling) reflects long-term incremental subsidence and the linear ridge
289 between faults B and C reflects long-term incremental uplift. Sediments are trapped as a
290 consequence of the linear ridge between faults B and C, and form a flat area on the south
291 side of fault C (Fig. 2d).

292 To the east of the junction of faults A and C, fault A has a relatively simple straight trace
293 across a terrace of the Cobanlı River. The ground surface to the north of the fault is
294 slightly folded up, forming a subtle anticline (the eastward continuation of the linear
295 ridge) that traps fine-grained sediments on the south side of the fault. The vegetation is
296 darker on the south side of the fault. Near the eastern end of the field area (Fig. 2a), field
297 observations indicate that saline water ponds are forming a salina on the south side of the
298 fault and travertine is forming on the north side of the fault.

299 **4. Paleoseismic trenching**

300 To investigate the variability of fault rupture lengths along the 1939 Erzincan Earthquake
301 fault rupture segment by comparing the results of paleoseismic investigations we require

302 long records of earthquake timing that incorporate as many seismic cycles as possible.
303 In-light of this objective, this study employs a paleoseismic trenching strategy to attain
304 the longest possible record of earthquake timing rather than focusing on collecting other
305 paleoseismic parameters such as offset per event and slip rate. In particular, this involves
306 undertaking trenches perpendicular to the fault and in locations with prolonged distinctive
307 and relatively continuous or frequent sedimentation that provide evidence for numerous
308 paleoearthquakes and can be safely exposed in a paleoseismic trench. These trenching
309 location attributes are traded-off against locations where piercing points might be
310 encountered that could yield rates of horizontal and vertical deformation.

311 We selected a number of potential paleoseismic trenching locations in the study area and
312 evaluated them by opening test-pits. Apart from test-pits across fault C, where we
313 encountered homogenous strata, all of the other test-pits were across fault A and many
314 were abandoned because of shallow groundwater (0.1 – 1.0 m below the surface). Four
315 test-pits were expanded into paleoseismic trenches and are labeled T1 to T4, from west to
316 east (Fig. 2a). Trenches T1 and T2 are located on the alluvial plain between the Cobanlı
317 River and Gunalan (Fig. 2b). Trench T3, by far the largest trench, was situated at the
318 base of the fault-bounded southern side of the elongate linear ridge in the inter-fan fine-
319 grained deposits (Fig. 2c). Trench T4 was about 2 m deep (to the top of the groundwater
320 table) and revealed evidence of two to four paleoearthquakes, which offset stratified,
321 thinly bedded (~5 cm) organic and inorganic deposits. Unfortunately, Trench T4 was
322 abandoned because of voluminous (estimated 5 l/s) discharge of unidentified gasses
323 which may have been detrimental to health. Therefore, trench T4 is not discussed further.

324 Paleoseismic trenches were logged in the field using a 1m x 1m (or smaller) string grid
325 on the trench walls and using a co-ordinate system (with the origin located below the
326 northern base of the trench). Stratigraphic units were logged, described and given unit
327 symbols. Photo mosaics of the trenches were made using photos taken during dispersed
328 lighting conditions. Photos were corrected for spherical divergence and crudely for the
329 geometry of the trench walls, but this is an imperfect process and is the reason for some
330 discrepancies between the trench logs and the photo mosaics. Further discrepancies may

331 also be due to small-scale erosion and cleaning of the trench walls between trench
332 logging and trench photography. We describe the results of each paleoseismic trench in
333 the following sections. We use the term ‘event horizon’ to describe a horizon that is
334 interpreted to correspond to a former ground surface (i.e. now buried) at the time of a
335 ground surface rupturing earthquake.

336 Paleoseismic trenches T1 and T2 revealed clear evidence of one and three
337 paleoearthquakes respectively. The more conventional evidence of paleoearthquakes in
338 paleoseismic trenches T1 and T2 are used to validate the less conventional evidence of
339 six paleoearthquakes revealed in paleoseismic trench T3. Because the number of
340 paleoearthquakes are relatively few in paleoseismic trenches T1 and T2, the age of the
341 event horizons are described along with the evidence of paleoearthquakes in Sections 4.1
342 and 4.2. Because the record of paleoearthquakes in paleoseismic trench T3 is longer and
343 the timing of earthquakes is validated by the findings of paleoseismic trenches T1 and T2,
344 this paleoearthquake timing record is described in the section 5. Paleoearthquake Timing.

345 ***4.1. Paleoseismic Trench T1***

346 Paleoseismic trench T1 was excavated to the top of the groundwater table on the alluvial
347 plain of the Cobanli River (Fig. 2). The trench revealed a faulted sequence of
348 interbedded clay (*Cn*), silty clay and clayey silt (*Fn*), sand (*Sn*) and organic soils (*Ps_n*)
349 overlying river gravel (*G_{xn}*). Figure 3 presents the trench log, Figure 4 presents a photo
350 mosaic of part of the east wall of the trench, and stratigraphic unit descriptions are
351 presented in Table A.A-1 (Annex A).

352 Trench T1 revealed clear evidence for one surface-rupturing earthquake (T1E0) based on
353 clear and multiple fault terminations at or near the base of sand unit S3. Based on this
354 interpretation, fault scarps formed following the event remained near vertical while unit
355 S3 was deposited. Cross bedding in sand unit S3 (above the event horizon) suggests that
356 it is an aeolian deposit, with the sand possibly blown from the bed of Cobanli River or
357 possibly reflecting an abundance of sand produced by liquefaction. This would explain
358 why the fault scarp or free-face remained intact while unit S3 was deposited, because if

359 the sand deposits were from a fluvial source one would expect the free-face to have been
360 more eroded.

361 Our interpretation is that the one event recorded in this trench is the 1939 Erzincan
362 earthquake. To confirm our interpretation we radiocarbon-dated a single sample (sample
363 37) from below the event horizon, which yielded a calibrated radiocarbon age of A.D.
364 1494 to present (2σ age range) (Table 2) (note. 'present' is used to reflect 1950 in
365 accordance with *Stuiver and Polach, 1977*). Therefore, paleoseismic trench T1 provides
366 evidence for one surface-rupturing earthquake that occurred on this segment of the fault
367 after sometime between A.D. 1494 and the present.

368 **4.2. Paleoseismic Trench T2**

369 Paleoseismic trench T2 was excavated down to the top of the groundwater table on the
370 alluvial plain of the Cobanlı River, closer to Gunalan than trench T1 (Fig. 2). The trench
371 revealed a faulted sequence of organic rich soils (*Psn*), sand (*Sn*), silt and clay (*Fn*),
372 gravel (*Gn*), with fissure infills (*In*) and liquefaction deposits (*Ln*). Figure 5 is a log of
373 both trench walls, Figure 6 is a photo mosaic overlain with the lines and labels of the
374 trench log, and stratigraphic unit descriptions are shown in Table A.A-2 (Annex A).

375 Trench T2 revealed evidence for three earthquakes, which we label from youngest to
376 oldest T2E0, T2E1 and T2E2. The youngest event, T2E0, has subtle evidence and
377 therefore evidence for T2E1 is described first. Event T2E1 is defined by fault
378 terminations that extend to the base of sand unit S6 on the east wall of the trench, (i.e.
379 Fig. 5, at horizontal distances 6.5 m and 8 m on the east wall). Coincident with these
380 fault terminations is a downward tapering wedge-shaped deposit on the east wall at a
381 horizontal distance of 12 – 13 m (Fig. 5) which we interpret as a fissure-fill deposit (I3).
382 The fissure fill deposit (I3) is interpreted to have formed in a tension crack opened due to
383 the folding of paleosols Ps1a and Ps1b down toward the fault and possibly associated
384 with some horizontal deformation. Evidence for the youngest event, T2E0, is restricted
385 to the fault zone on the west wall (at ~7 m on the horizontal axis) where there are two
386 fissure fill deposits (I1 and I2) that rest on a block of sand units (sand units S8-4) between

387 two fault strands. The fault strand on the southern side of these deposits extends to the
388 top of S4 which is a higher stratigraphic level than the faults on the east wall. Together,
389 these observations suggest that the top of unit S4 is an event horizon, which we label
390 event T2E0, and that the base of sand unit S6 is also an event horizon, which we label
391 event T2E1. Unfortunately, T2E0 is only evidenced on the west wall, which
392 considerably weakens the strength of our interpretation. Event T2E2 is evidenced by
393 increasing deformation with depth. North of the fault zone on the west wall, paleosol
394 Ps2a is folded down towards the fault, whereas the overlying paleosols are flatter lying.
395 Between the fault strands, at around a horizontal distance of 7 m on the east wall,
396 paleosol Ps2 is also folded down toward the fault and is overlain by fine grained
397 sediments and sand layers that thin to the north indicating onlap on to a folded surface.
398 Units between and including F1 and S9 exposed on the southern side of the northern most
399 fault strand on the east wall appear to have deposited onto a folded Ps2a (i.e. they thin to
400 the north). Therefore, event horizon T2E2 can be constrained to between units Ps2a and
401 F1. We interpret the top of Ps2 to be a fault-zone angular unconformity. Therefore, we
402 consider the top of paleosol Ps2a to be the event horizon that corresponds to event T2E2.

403 Liquefaction deposits were recognized on both walls of the trench. It is assumed that the
404 source layer(s) for the liquefaction deposits is below the strata exposed in this trench. L2
405 is a horizontally bedded sand deposit with pebble horizons that rests on top of Ps2a. L2
406 is only exposed for ~2m on the trench wall and becomes laterally finer and eventually
407 indiscernible from Ps1b. Near the centre of the horizontal extent of L2, the deposit
408 contains more pebbles, less bedding, and below its center it connects to the upper part of
409 a feeder dike that cross-cuts Ps2a. We interpret L2 as a surficial sand blow deposit,
410 which provides additional evidence that the top of Ps2a is an event horizon (T2E2).
411 Liquefaction deposit L1 is a sub-vertical dike that terminates upward in Ps1b and cross-
412 cuts L2, which is also faulted (at a horizontal distance of 6.5 m on the east wall). There is
413 no evidence that this dike reached the surface, so it cannot be tied to a particular event
414 horizon; however, it clearly occurred subsequent to T2E2 because of cross-cutting
415 relations. We attribute the liquefaction deposit L1 and the faults that offset liquefaction
416 deposit L2 to either of the younger events T2E0 or T2E1.

417 To constrain the age of the three event horizons in trench T2, seven samples were
418 radiocarbon-dated; details of the radiocarbon data and the units from which they were
419 sampled are presented in Table 2. Samples 40 and 47 are clearly reworked as they are
420 substantially older than the other sample ages, which suggests that paleosol Ps1b
421 comprises a significant component of reworked soils. Samples 41 and 42 (both from
422 paleosol PS1a) are the highest in the strata and provide the maximum age of both events
423 T2E0 and T2E1. Both samples 41 and 42 have similar 2σ calibrated age ranges of ~ A.D.
424 1660 to present, indicating that the two most recent earthquakes (T2E0 and T2E1)
425 occurred after sometime between A.D. ~1660 and the present (i.e. 1950). The minimum
426 age of event T2E2 is constrained by sample 50, and the maximum age by samples 43 and
427 49, which are very similar. Therefore, event T2E2 occurred sometime between A.D. 200
428 and A.D. 1640.

429 ***4.3. Paleoseismic Trench 3***

430 Unlike paleoseismic trenches T1 and T2, paleoseismic trench T3 was excavated to about
431 5 m depth and did not encounter groundwater. The trench revealed an interfingering
432 sequence of stratigraphic units comprising of: gravel (*Gn*, *Rg*, *Rgn*, *UG*, or *Ga*), gravel
433 wedges (*Gnx*), sand layers (*Sn*), organic rich soils (*Psn*) and fine-grained deposits (i.e.
434 various mixtures of silt and clay) (*Fnx*). We interpret that these stratigraphic units were
435 deposited in a similar environment as found at the site today which is a small inter-
436 alluvial-fan wet-land at the base of a fault scarp. During the period of deposition the
437 trench location may have evolved subtly; in particular the wetness of the site due to
438 climate, and/or tectonic and anthropogenic influences on drainage paths. Trench 3 was
439 oriented perpendicular to the strike of the fault A (Fig. 2) at the base of a steep (~30°)
440 south-facing slope (the southern side of the elongate linear ridge) composed of Pliocene
441 clastic deposits (*Kocyigit* 1990) that we describe as a poorly sorted gravel with silt to
442 boulder-sized clasts. The strategy for trenching at this location was to find evidence of
443 multiple fault ruptures (reflecting paleoearthquakes) in an area with regular and relatively
444 continuous sedimentation. This location also had the advantage that different sediments
445 are present on either side of the fault, gravels to the north and inter-alluvial-fan wetland

446 sediments (organics and distal fan deposits) on the south side of the fault; this can assist
447 with the interpretation of the origin of strata in the fault zone.

448 Figure 7 is a log of Trench T3, Figure 8 is a photo mosaic overlain by the lines and
449 annotation from the trench log, and Table A.A-3 (Annex A) provides the stratigraphic
450 unit descriptions. The trench walls were benched with upper and lower walls separated
451 by an ~1 m wide bench (Fig. 7). The distance between the bases of the lower walls was
452 ~3 m.

453 *Fine-grained deposits*

454 Fine-grained deposits are composed of silt and clay and are interpreted to be distal
455 alluvial fan deposits. We interpret that these deposits were laid down relatively slowly by
456 deposition of suspended load in flood waters sources from the low hills to the south of the
457 trench site. This interpretation is consistent with the northward tapering geometry of
458 these units where they interfinger with gravel wedges. The fine-grained soils may have
459 included organic rich layers but the decomposition of the organic component of such soils
460 has rendered them indistinguishable from the fine-grained deposits below approximately
461 1m below the ground surface. Organic rich soils in the top one meter of the trench are
462 interpreted to be paleosols formed at the present ground surface (i.e. 'Topsoil' Fig. 7) or
463 at former, now buried, ground surfaces (i.e. 'Ps1' and 'Ps2' Fig. 7).

464 *Sand Deposits*

465 Distinctly continuous and recognizable (in the field) thin beds and laminae of sand (1 to
466 300mm thick) were logged on both walls of the trench and provide very useful marker
467 horizons in the strata. The sand layers are interbedded with the fine-grained and organic
468 rich strata in the south of the trench and also interfinger with gravel wedges towards the
469 northern end of the trench. Five sand layers were recognized on the west wall of the
470 trench (S1 – S5), which correlate to sand layers on the east wall with the exceptions of
471 the absence of sand layer S3 and the additional deeper sand layer S6 on the east wall.
472 The origin of the sand layers remains uncertain. They may have been deposited by flood

473 waters from the alluvial fans, by aeolian processes or perhaps they are associated with
474 liquefaction on the less distal parts of the alluvial fan. It is unlikely that all of the sand
475 layers are caused by liquefaction which we establish below because most of the sand
476 layers do not correspond with other evidence for paleoearthquakes.

477 The sand layers illustrate a clear increase in dip, down to the south, with depth.
478 Regardless of the process of deposition that formed the sand layers, if they had been
479 deposited on a slope with the angle near the base of the trench we would expect to see an
480 increased thickness away from the fault. Therefore, this dip must have formed after
481 burial as a consequence of tectonic deformation. The sand units are steeper near the fault,
482 but south of a horizontal distance of ~10 m the sand layers S1 and S2 are horizontal,
483 whereas S4, S5, and S6 dip at 4° to 7°. Unfortunately, there are no horizons that we can
484 justifiably measure the angle of between S2 and S4, and therefore we can not use the
485 change in dip to identify event horizons. Nonetheless, the increasing dip of bedding with
486 depth indicates that significant syndepositional tectonic deformation has been occurring
487 while this sedimentary sequence has been deposited. It also indicates that there is a down
488 to the south displacement of the fault and this indicates that the genesis of the elongate
489 ridge described in Section 5 does include some recognizable component of dip-slip
490 displacement over time.

491 *Gravel Deposits*

492 Numerous gravel units have been described in this trench in accordance with their
493 properties and the interpretation of their origin. Stratigraphic descriptions are provided in
494 Table A.A-3 (Annex A). The gravel units have been partitioned into five groups as
495 follows:

496 1. River gravels (Rg and Rgn)

497 River gravels are interpreted to be much older than the other gravel units exposed
498 in the trench due to their intense deformation. We correlate this unit to Pliocene
499 continental clastics (Cobanlı Group) which form the scarp to the north of the

500 trench (Koccyigit, 1990 pg.157). This unit may be equivalent to the structureless
501 gravel (Ga).

502 2. Undifferentiated gravels (UG)

503 This symbol is used for areas where no structure is recognizable due to
504 bioturbation but the material is interpreted to be equivalent to the ‘distinctive
505 gravel units (Gn)’ and perhaps ‘gravel wedges (Wn and Wnx)’.

506 3. Distinctive gravel units (Gn)

507 Particular distinctive gravel colluvium deposits sourced from the slope to the
508 north of the fault. Many of these units are probably equivalent to the ‘gravel
509 wedges (Wn and Wnx)’ but due to the extensive faulting, which probably includes
510 significant (but unquantified) lateral displacement, and lateral variability in unit
511 thickness and composition, these are seldom correlated across the fault. Many of
512 the units represent undifferentiated combinations of differentiated units (e.g. unit
513 G2 is undifferentiated units G1 and G3). Gravel unit G13 is interpreted as a
514 fissure-infill based on its structure.

515 4. Structureless gravel (Ga)

516 This gravel has no coherent internal structure. It is possible that this unit is a very
517 large ‘gravel wedges (Wn and Wnx)’ unit; however it is more likely that this is
518 equivalent to the ‘River gravels (Rg and Rgn)’.

519 5. Gravel wedges (Wn and Wnx)

520 Gravel wedges are wedge shaped stratigraphic units that interfinger with the fine-
521 grained, organic rich and sand deposits to the south. These wedges are composed
522 of a range of materials but mostly reworked ‘river gravels (Rg and Rgn)’ and are
523 interpreted to be colluvial wedges. Each gravel wedge is given a sub number (n)
524 which are correlated to the equivalent unit on the opposite wall, where the
525 materials are different a further sub-number (x) is used to provide separate
526 stratigraphic unit descriptions.

527 *Tectonostratigraphy*

528 Two tectonostratigraphic features are used to identify the location of event horizons; fault
529 terminations and colluvial wedges. Because of the difficulty of distinguishing the extent
530 of faults in gravel deposits (along with evidence of bioturbation) we have a low level of
531 confidence for the stratigraphic location of fault terminations in this trench. We have
532 only logged the location of faults where we were confident of their presence. In response
533 to this low level of confidence fault terminations are only used as corroborating evidence
534 for event horizons and we rely more heavily on colluvial wedges.

535 A colluvial wedge is a deposit formed on the downthrown side of a fault by collapse of a
536 fault scarp (free face) during or soon (i.e. years to tens of years) after an earthquake. The
537 base of a colluvial wedge can be interpreted an earthquake event horizon. We interpret
538 many of the 'gravel wedges (W_n and W_{nx})' to be colluvial wedges linked to ground
539 rupturing earthquakes. Arguably, these colluvial wedges could be formed by localized
540 failures of the steep slope to the north of the trench caused by non-seismic processes such
541 as extreme rainfall events. Because the south-facing steep slope comprises a loose gravel
542 deposit that has very little cohesion and negligible tensile strength, localized slope
543 failures are likely to be small (i.e. $<2 \text{ m}^3$) and therefore their associated deposits at the
544 base of the slope would not be laterally continuous. Colluvial wedges caused by surface
545 rupturing earthquakes are expected to be more laterally continuous.

546 Colluvial wedges could be formed by two processes related to fault rupture, fault scarp
547 retrogression (scarp collapse and subsequent erosion up the slope) and widespread slope
548 failures caused by seismic shaking (ground acceleration). Both of these processes could
549 mobilize a significant volume of gravel from the steep slope. We suspect that widespread
550 slope failure as a consequence of high ground accelerations are the cause of the gravel
551 wedges, because we do not see significant evidence of vertical displacement in the fault
552 zone (although this is not quantifiable in a single trench across a strike-slip fault). A
553 similar approach has been used to identify paleoearthquakes at two other locations on the
554 North Anatolian Fault (*Fraser et al.* 2009a & 2010b). To distinguish localized slope
555 failure deposits from colluvial wedges we considered opening two trenches on this
556 section of the scarp so that lateral continuity of gravel wedges could be assessed.

557 However, groundwater was encountered at less than 1 m depth in nearby test-pits so
558 trench T3 was made as wide as practical, with the upper walls ~5 m apart and lower walls
559 ~3 m apart. South of the fault zone above gravel (Ga) we recognize seven distinct gravel
560 wedges, all of which are present on both walls of the trench. We interpret that gravel
561 wedge W1 is a consequence of constructing a road along the slope immediately north of
562 the trench (Fig. 2e). The remaining six gravel wedges are interpreted to be seismogenic
563 colluvial wedges.

564 The amount of horizontal offset cannot be constrained in this trench. The amount of
565 vertical offset is not discussed as it cannot be used as evidence for displacement rates
566 because of the unknown horizontal displacement and the potential range of orientations
567 of any particular stratum.

568 The evidence for six paleoearthquake events which we label T3E0 – T3E5 youngest to
569 oldest respectively are described below. The event horizons are shown and labeled in
570 Figures 6 and 7 and stratigraphic unit descriptions are provided in Table A.A-3 (Annex
571 A).

572 Paleoearthquake T3E0

573 Evidence for this event is a small colluvial wedge (gravel wedge W2) which is
574 much more clearly evident on the west wall than the east wall where gravel
575 wedges W1 and W2 were not differentiated. Corroborating evidence is provided
576 by two fault terminations at the base of gravel wedge W2 at a horizontal distance
577 of ~4m on the west wall. Supporting evidence for an event horizon at this
578 stratigraphic position is an offset of the base of the preceding event horizon
579 (T3E1) at a horizontal distance of approximately 5m on the west wall.

580 Paleoearthquake T3E1

581 This event corresponds to the base of the colluvial wedge W3. A fault
582 termination at the base of of colluvial wedge W3 at a horizontal distance of
583 approximately 4.5 m on the west wall provides corroborating evidence for this
584 event horizon. On the east wall of the trench there is a lack of distinctive strata

585 immediately south of the fault zone making interpretation difficult. Because
586 gravel wedge W3 lies between sand S2 and gravel wedge W4a to the south of the
587 fault zone the event horizon is projected into the fault zone on the east wall along
588 the top of the distinctive unit W4a. This shows an additional fault termination at a
589 horizontal distance of ~5.75 on the east wall.

590 Paleoearthquake T3E2

591 Gravel wedge W4 is composed of three distinct units (W4a, W4b and W4c) and
592 collectively this wedge is larger than the younger wedges. On the west wall of the
593 trench this event horizon is corroborated by fault terminations at a horizontal
594 distance of 7m and if we assume that gravel unit G3 corresponds to gravel wedge
595 W4c there is a fault termination at a horizontal distance of ~2m that offsets the
596 event horizon. Since gravel unit G2 is undifferentiated gravel units G1 and G3,
597 fault terminations at its base at horizontal distances of ~3.75m and 4.75m on the
598 east wall may also be considered as corroborating evidence for this event horizon.
599 The termination at a horizontal distance of ~4.75m may pass through the event
600 horizon by several cm, this may reflect a small amount of slip associated with a
601 subsequent non surface rupturing event, or a lack of evidence for faulting due to
602 bioturbation above the event horizon, or postseismic slip. The fault termination at
603 a horizontal distance of ~3.75m on the east wall offsets the event horizon which
604 suggests that the offset occurred post deposition of the gravel above the event
605 horizon at this location (i.e. by a subsequent event). The apparent thrust
606 displacement is attributed to strike-slip displacement as the event horizon T3E3
607 below is not vertically offset.

608 Paleoearthquake T3E3

609 The gravel wedge W5 is interpreted to have formed as a result of this event and its
610 base is interpreted to be the event horizon T3E3. Gravel wedge W3 is composed
611 of two distinguishable units on the east wall (W5a and W5b) while only the lower
612 unit (W5b) is present on the west wall. The event horizon is also defined as the
613 contact between gravel units G7 and G9. At some locations these are

614 indistinguishable and are collectively labeled G8. For example, G8 is present
615 between horizontal distances ~3.25m and ~5.25m on the west wall of the trench
616 and in this area we cannot identify the event horizon. A fault terminates just
617 below the event horizon at a horizontal distance of ~6.25m on the east wall of the
618 trench, this may correspond to the event that formed gravel wedge W5 but it is not
619 definitive. There is relatively little corroborating evidence for this event horizon.

620 Paleoearthquake T3E4

621 This event horizon is defined as the base of gravel wedge W6 which has a similar
622 geometry on the trench wall to that of the gravel wedges up-sequence. No fault
623 terminations are recognized at this event horizon. The equivalent gravel units in
624 and north of the fault zone cannot be correlated to the gravel wedge W6. This is
625 attributed to lateral offset which is probably quite significant if there has four
626 subsequent, predominantly strike-slip, surface-rupturing earthquakes on this
627 segment.

628 Paleoearthquake T3E5

629 The evidence for this event is a colluvial wedge (gravel wedge W7) which is
630 notably smaller than many of the wedges in the up-sequence stratigraphy. There
631 is also no corroborating tectonostratigraphic evidence for this event horizon, just
632 the formation of a colluvial wedge.

633 Further validation of the evidence for the event horizons can be found by comparison of
634 the ages with the events identified in paleoseismic trenches T1 and T2 and the results
635 from other paleoseismic studies undertaken on nearby sections of the North Anatolian
636 Fault.

637 **5. Paleoearthquake timing**

638 To constrain the age of the event horizons established using colluvial wedges in trench
639 T3, we radiocarbon-dated 16 charcoal samples and 14 bulk samples (Table A.B-1, Annex
640 B). The bulk samples were processed to extract pollen, but at a late stage in the process

641 we found that there would not be enough pollen to date. Therefore, the dated materials
642 comprised 40-63 μm sized organics dominated by micro charcoal and pollen fragments
643 (see Annex B for a description of the processing procedure). As is common when many
644 samples are dated in a sedimentary sequence, many of the sample ages are inconsistent
645 with their relative stratigraphic positions (e.g. *Hartleb et al.*, 2003; *Fraser et al.*, 2009a;
646 *Fraser et al.*, 2010b). It is difficult to distinguish between reliable and unreliable sample
647 ages. However, a parsimonious approach was taken, whereby the least samples were
648 excluded to establish a stratigraphically logical sequence of sample ages. Eight samples
649 are interpreted as too old relative to adjacent sample ages. This is attributed to reworking
650 of sample material from the southern face of the elongate linear ridge and alluvial fans
651 and their catchments. Four of the samples are interpreted as too young relative to the
652 adjacent sample ages, which is attributed to bioturbation although the fine-grained
653 deposits may also be prone to desiccation cracking, which would provide conduits for
654 organic material to be washed into the subsurface (i.e. creating an anomalously young age
655 in the stratigraphic unit in which it is deposited).

656 Using the remaining 18 samples, we made an order-constrained Bayesian model
657 (electronic supplement 1) using the software OxCal (*Bronk Ramsey*, 2007) to derive
658 modeled probability density functions (PDFs) of the sample and earthquake ages (Table 2
659 and Fig. 9). Where multiple samples from a stratigraphic unit are incorporated in the
660 Bayesian model, they are grouped into “phases” (relative order unspecified), and these
661 phases were grouped into a sequence along with the individual samples from stratigraphic
662 units (i.e. not in a ‘phase’) according to their stratigraphic order. The order-constrained
663 Bayesian model has a model index of 91 (*Bronk Ramsey*, 2007), which exceeds the
664 recommended 60 for a conformable model.

665 The order-constrained Bayesian model was also used to determine the PDFs of the inter-
666 event time, the summed inter-event time, and the average recurrence interval (Table 3)
667 (i.e. using the same methodology as *Fraser et al.* 2010b and *Lienkaemper and Bronk*
668 *Ramey* 2009). The inter-event time is the period between two earthquakes expressed as a
669 PDF that accounts for the uncertainty in the timing of the earthquakes. The summed

670 inter-event time is the normalized sum of the inter-event times and provides a very good
671 description of the probable time between earthquakes, taking into account both the
672 natural variation in recurrence interval and the uncertainty associated with constraining
673 the age of earthquakes. The average recurrence interval is simply the period between the
674 youngest (T3E0: 1939 Erzincan earthquake) and the oldest event (as a PDF) divided by
675 the number of inter-event times, in this case 5.

676 The Bayesian model for trench T3 provides by far the best earthquake record of the three
677 trenches, although the data are complimentary to the findings of T1 and T2. Trench T1
678 informed us that one earthquake (T1E0) occurred after deposition of sample 37 (CRA:
679 A.D. 1494 – A.D. 1951 2σ), which is consistent with trenches T2 and T3. Trench T2
680 informed us that two earthquakes happened after ~ A.D. 1660 using only the highest two
681 samples below two event horizons (T2E0 and T2E1). This is consistent with trench T3
682 where we interpreted the ultimate event as the 1939 Erzincan earthquake (Table 2), and
683 the age of the penultimate event (T3E1) is constrained to between A.D. 1408 and A.D.
684 1804. The information from trench T2 strongly suggests that the penultimate event
685 (T2E1) occurred between ~ A.D. 1660 and A.D. 1804. The third event horizon identified
686 in trench T2 (T2E2) was constrained to sometime between A.D. 200 and A.D. 1640,
687 consistent with the event T3E2 (A.D. 1254 – A.D. 1391) from trench T3, but far less
688 precise. The good correlation between the three trenches provides some significant
689 validation to the link between formation of gravel wedges in trench T3 and other types of
690 evidence of paleoearthquakes revealed in trenches T1 and T2. Older paleoearthquakes
691 determined in trench T3 are summarized in Table 2.

692 Because event T3E0 corresponds to T2E0 and T1E0, and T3E1 corresponds to T2E1 and
693 so on, hereafter we label the events E0, E1, E2, et cetera.

694 **6. Spatiotemporal Fault Rupture Correlation**

695 This discussion focuses on comparing the earthquake record established in this study
696 (Table 2) to paleoearthquake chronologies from four other paleoseismic investigations on

697 the 1939 Erzincan earthquake rupture segment (*Hartleb et al.*, 2006, Fraser, 2009b and
698 *Kozaci et al.*, 2011) and with to the record historical earthquakes (Table 1). Table 4
699 summarizes correlations which are presented graphically in Figure 10.

700 Gunalan is located near the western end of the Mihar-Tumekar fault segment (*Barka*,
701 1996, Fig. 1), Resadiye (*Fraser*, 2009b) is located on the Kelkit Valley fault segment
702 ~130 km west of Gunalan, and Yaylabeli (*Kozaci et al.*, 2011) and Cukurcimen (*Hartleb*
703 *et al.*, 2006) which are located near the eastern end of the Mihar-Tumekar fault segment
704 are 27 km and 31 km east of Gunalan, respectively.

705 To use paleoearthquake timing data to investigate if previous earthquakes have had the
706 same extent of fault rupture as the 1939 Erzincan Earthquake two assumptions are made:

- 707 1. Where paleoearthquakes are dated to around the same time at multiple locations
708 on the fault rupture segment they reflect a single earthquake. However, this
709 assumption may erroneously group surface rupturing earthquakes that occur
710 closely spaced in time (relative to the age constraint determined in paleoseismic
711 investigations).
- 712 2. Where paleoearthquakes are not present in the stratigraphy at one location, but
713 they are at others, then only part of the fault rupture segment ruptured. This
714 assumption may be erroneous where paleoseismic investigation provides an
715 incomplete paleoearthquake record; this is very difficult to prove or disprove.

716

717 All of the studies on the 1939 rupture segment recognize evidence of the 1939 Erzincan
718 earthquake (*Fraser*, 2009b; *Hartleb et al.*, 2006; *Kozaci et al.*, 2011) which is consistent
719 with the extent of the fault rupture segment described by *Barka* (1996). In this study, the
720 1939 earthquake is interpreted to be E0 but due to the imprecision of radiocarbon dating
721 in the last few hundred years this remains an assumption.

722 In trench T3, event E1 was constrained to A.D. 1408 – .A.D 1804, which corresponds to
723 the timing of 10 possible historical earthquakes (Table 1). However, Trench T2 indicates

724 that this event occurred after ~A.D. 1660, reducing the possible correlative events to
725 earthquakes in A.D. 1668, 1684, and 1754 (Table 1). This event is interpreted to
726 correlate to one of the three major earthquakes that were reported in A.D. 1668
727 (*Ambraseys and Finkel, 1995; Ambraseys and Jackson, 1998; Sengor et al., 2005*). This
728 earthquake was also recognized at Resadiye (*Fraser, 2009b*), but not in the trenches to
729 the east of this study (*Hartleb et al., 2006; Kozaci et al., 2011*). This suggests that the
730 Mihar-Tumekar fault segment (Fig. 1c) identified by Barka (1996) does not always
731 rupture in unison (i.e. it may comprise of more than one fault segment). Although the
732 evidence of offset associated with the .A.D 1668 event at Gunalan may be interpreted as
733 spillover displacement from the Ortakoy-Susehri segment that terminates about 10 km
734 west of Gunalan (i.e. Gunalan is near a slip patch transition (*Sieh, 1996*)).

735 Event E2 was constrained to the period A.D. 1259 – A.D. 1391 using the data from
736 trench T3 (the results from trench T2 provide a poorer temporal constraint), which may
737 correlate to one of three historical earthquakes that occurred in A.D. 1254, 1287, and
738 1374 (Table 1). Notably, the A.D. 1254 earthquake occurred just outside the 2σ age
739 range for E2 established in this study. However, because the A.D. 1254 event was also
740 recognized at Yaylabeli (*Kozaci et al., 2011*) and Cukurcimen (*Hartleb et al., 2006*) and
741 was reported widely along the 1939 rupture segment in historical records (*Ambraseys and*
742 *Jackson, 1998; Guidoboni and Comastri, 2005*), we interpret that E2 corresponds to this
743 earthquake. The A.D. 1254 earthquake was not recognized at Resadiye (*Fraser, 2009b*),
744 which suggests that this earthquake ruptured an eastern portion of the 1939 Erzincan
745 earthquake rupture segment with its western termination located somewhere between
746 Resadiye and Gunalan.

747 Event E3 was constrained to A.D. 241 – A.D. 644 in trench T3, which correlates with
748 timing of three historical earthquake records: (1) vague reports of an earthquake in the
749 3rd, 5th and 7th centurys A.D. from Amasya, Niksar and Nicopolis (*Ambraseys, 1970*); (2)
750 an earthquake was reported in A.D. 499 in Niksar and Nicopolis (*Ambraseys and*
751 *Jackson, 1998; Guidoboni and Comastri, 2005*); (3) an earthquake that reportedly
752 destroyed Niksar in A.D. 343 (*Guidoboni et al., 2005*). Historical earthquake (1) does

753 not necessarily provide evidence for a ground surface rupturing earthquake while
754 historical earthquake (3) is reported only near Niksar which may reflect an earthquake
755 with a rupture similar to the 1942 Niksar Earthquake (Fig.1b shows extent of this rupture)
756 which did not rupture the 1939 rupture segment. The A.D. 499 earthquake was
757 recognized in all of the paleoseismic studies on the 1939 rupture segment. We interpret
758 that Event E3 corresponds to the historical A.D. 499 earthquake. This suggests that the
759 A.D. 499 earthquake was similar in extent to the 1939 earthquake, although further
760 paleoseismic data from the Erzinazari fault segment is required to validate this
761 interpretation.

762 Notably, there was a long period of time between the A.D. 499 (E3) earthquake and the
763 subsequent earthquake (E2) in A.D. 1254 recognized at Gunalan. Over that period no
764 earthquakes were recognized at Resadiye (*Fraser, 2009b*), whereas the two studies to the
765 east both recognized an earthquake in A.D. 1045 (*Hartleb et al., 2006; Kozaci et al.,*
766 *2011*) and another event was recognized at Yaylabeli at A.D. 710 – A.D. 850 (*Kozaci et*
767 *al., 2011*). Again, this suggests that there is a fault rupture segmentation boundary
768 between Gunalan and Yaylabeli. Alternatively, it is possible that these events were
769 spillover displacements from the Erzincan fault segment (Fig. 1c).

770 Event E4 was constrained to the period 881 B.C. – 673 B.C. which does not correlate to
771 any earthquakes in the historical record. Event E4 corresponds to an earthquake
772 identified at Resadiye that was constrained to the period 908 B.C. – 702 B.C. (*Fraser,*
773 *2009b*), but the paleoseismic record from Yaylabeli (*Kozaci et al., 2011*) does not extend
774 beyond the A.D. 499 earthquake. The Cukurcimen study identified an event at 1450 B.C.
775 – 800 B.C. which may correspond to this event, but the large age bracket overlaps more
776 with the timing of E5.

777 Between events E3 and E4 an event was identified both west of our trenching site at
778 Resadiye (*Fraser, 2009b*) and to the east at Cukurcimen (*Hartleb et al., 2006*) (Table 1).
779 The absence of this event in trench T3 suggests that either this paleoearthquake did
780 rupture the fault at Gunalan and no evidence was preserved in our trench, or that it

781 corresponds to two separate paleoearthquakes that occurred at around the same period on
782 each end of the 1939 rupture segment.

783 Event E5 (1406 B.C. – 1291 B.C.) is interpreted to correspond with the oldest event
784 identified at Cukurcimen (*Hartleb et al.*, 2006). Although the 2σ range of E5 does not
785 overlap with 1200 B.C., this event may correspond to an earthquake, or series of
786 earthquakes (like that of the 20th Century), that may have occurred around 1200 B.C.
787 (*Nur and Cline*, 2000). The occurrence, timing, and extent of damage associated with
788 this earthquake is relatively speculative and based on archaeological evidence. This
789 event was not identified at Resadiye (*Fraser*, 2009b), which suggests that the earthquake
790 fault rupture stopped somewhere between Gunalan and Resadiye. Notably, the
791 paleoseismic record at Resadiye identified two older earthquakes (Table 4)

792 Figure 9b presents the inter-event times (IET), which are summarized in Table 3. IET0-1
793 corresponds to the interval between events E0 and E1, IET1-2 to the interval between
794 event E1 and E2, et cetera. If our correlation of paleoearthquakes to historical earthquakes
795 are correct, then IET0-1 is 271 years, IET1-2 is 414 years, and IET2-3 is 755 years; the
796 older events were not matched to historical earthquakes. These correlative IETs fall
797 within the IET PDFs determined from our paleoseismic data. The summed inter-event
798 time (SIET), calculated using only paleoseismic data from Gunalan, has a broad 2σ range
799 of 109 – 1385 years, which is very similar to the 0 – 1375 years determined at Resadiye
800 (*Fraser*, 2009b). The summed inter-event time at Resadiye (*Fraser*, 2009b) was found to
801 be bimodal with modes at 100 – 400 years and 900 – 1200 years, which was speculatively
802 attributed to two typical sized earthquakes that rupture the Kelkit valley segment of the
803 NAF. At Gunalan there is a weaker bimodality. The longer SIET mode is due to two
804 long inter-event times between E2 and E3, and between E3 and E4. This suggests a
805 relatively variable period between large earthquakes. Fraser et al. 2010a use these data
806 along with order-constrained Bayesian models for paleoseismic investigations along the
807 entire North Anatolian Fault to investigate spatial temporal patterns of paleoearthquakes.

808 **6.1. Paleearthquake Magnitude Estimation**

809 Assuming that the paleoseismic investigations identified a continuous (complete) record
810 of earthquakes locally, the fault segments that comprise the 1939 Erzincan earthquake
811 fault rupture segment do not always rupture in tandem. By roughly estimating the length
812 of fault rupture associated with paleoearthquakes we estimate their magnitude. Figure 10
813 graphically summarizes the length of rupture associated with paleoearthquakes described
814 in the previous section and summarized in Table 4.

815 Using the length of rupture of the paleoearthquakes based on paleoseismic investigations
816 and the fault segmentation proposed by Barka (1996), we estimate the length of rupture
817 for the paleoearthquakes correlated between investigation sites in Table 4. Using an
818 empirical equation ($M_w = A + B \log L$) that relates length of rupture (L) and regression
819 coefficients (A – Y intercept and B – regression slope) to moment magnitude (M_w) (*Wells*
820 *and Coppersmith*, 1994) we estimate the moment magnitude (M_w) of the
821 paleoearthquakes and rupture of the individual fault segments proposed by Barka (1996).
822 The 1σ limits of the regression coefficients ($A=5.16\pm 0.13(1\sigma)$, $B=1.12\pm 0.08(1\sigma)$)
823 provided by *Wells and Coppersmith*, 1994 are used to estimate the maximum and
824 minimum moment magnitudes. This estimate assumes that the fault segment boundaries
825 identified by Barka (1996) are valid in most cases. The magnitudes estimated for the
826 possible fault rupture segment lengths associated with paleoearthquakes (summarized in
827 Table 8) all exceed M_w 7.0, which suggests that shorter ruptures along the 1939 Erzincan
828 earthquake rupture segment also produce large magnitude earthquakes.

829 **6.2. Fault Rupture Cycles**

830 Figure 10 graphically summarizes the rupture lengths and our estimated magnitudes. An
831 important observation is that we do not recognize a cyclical pattern of earthquakes. The
832 number of paleoseismic studies along the 1939 fault rupture segment is not great enough
833 to make any definitive conclusions. Further studies are particularly required on the
834 Ezinepazari, Ortakoy-Susehri and Erzincan fault segments.

835 Sieh (1996) describes fault segments (map-view) as ‘patches’ in terms of a three-
836 dimensional section of a fault plane. He documents examples where “adjacent individual

837 patches, 10 km or more in length, failed singly during one event and in tandem during the
838 other” and found that “...large earthquakes commonly result from the failure of one or
839 more patches, each characterized by a slip function that is roughly invariant through
840 consecutive cycles” (Sieh, 1996 p. 3764) with the exception of transition zones between
841 slip patches, where slip may deviate from event to event. With the data available from
842 the paleoseismic studies along the 1939 Erzincan Earthquake rupture segment we are not
843 able to determine if any of the sites are at the transition zones between slip patches. It
844 would therefore be advantageous to understand the amount of slip during
845 paleoearthquakes along the 1939 rupture segment.

846 Fraser *et al.* (2010a) described the behavior of the eastern sections of the NAF as
847 bimodal, with two apparent typical periods between paleoearthquakes. The variable time
848 between earthquakes, the time-variable fault rupture length and hence the variable
849 earthquake magnitude could be due to the intermittent effect of contagion. Fault-rupture
850 contagion is where the rupture of one fault or fault segment increases the likelihood of the
851 occurrence of rupture on an adjacent fault or fault segment (Perkins, 1987). “Under
852 certain conditions, the [fault] system can behave as a two-stage process: one stage having
853 a high recurrence rate [i.e. frequent earthquakes] during the contagion processes and a
854 second stage having a long, quiescent inter-contagion time.” (Perkins, 1987, p. 429). In
855 the case of the 1939 fault rupture segment, contagion could be associated with adjacent
856 fault segments of the NAF or from other faults. By investigating spatiotemporal patterns
857 of seismicity using paleoseismic data from southern California, Dolan *et al.* (2007) found
858 that seismicity on one fault system can suppress seismicity on another fault system that
859 accommodates the same plate boundary motion. Such a relationship between the NAF
860 and for example, one or a combination of the EAF, NEAF, OF, AIF, (Fig.1a) or other
861 faults, may affect the spatiotemporal distribution of earthquakes on the eastern section of
862 the NAF (Fraser *et al.* 2010a). This can also be considered in terms of stress transfer.
863 Stein *et al.* (1997) found that stress changes induced by fault rupture of adjacent fault
864 strands, or other faults, may increase the likelihood of rupture on a particular section of
865 the NAF.

866 Barka (1996) notes that “The 20 November 1939 Tercan earthquake, an $M = 5.9$ event
867 that occurred 5 weeks before the 1939 Erzincan earthquake on the NE-SW striking
868 Northeast Anatolian fault, is considered to be a preshock of the 1939 Erzincan
869 earthquake” (p. 1240). This suggests that there may be some degree of behavioral
870 coupling between these fault systems in terms of triggering, but does not provide
871 evidence of coupling in terms of long-term behavior. To address this further, studies on
872 adjacent fault systems such as the NEAF, Alf and OF are required to provide long records
873 of paleoearthquakes.

874 **7. Conclusions**

875 A paleoseismic investigation was undertaken on the 1939 Erzincan earthquake rupture
876 segment of the North Anatolian Fault (NAF) near the village of Gunalan between
877 preexisting investigations at Resadiye (*Fraser et al.*, 2009b) to the west and Yaylabeli
878 (*Kozaci et al.*, 2011) to the east. The investigation comprised three paleoseismic
879 trenches. Trenches T1 and T2 were excavated on the alluvial plain of the Cobanlı River.
880 Trench T1 revealed clear evidence for one earthquake after ~ A.D. 1494 which is
881 interpreted to be the 1939 Erzincan earthquake. Trench T2 revealed evidence of two
882 earthquakes near the top of the trench that both occurred sometime after ~A.D. 1660, one
883 of which was interpreted to be the 1939 Erzincan earthquake. A third event in trench T2
884 was constrained to A.D. 200 – A.D. 1640. Trench T3 revealed a record of colluvial
885 wedges that interfinger with fine-grained inter-fan deposits. We interpreted a sequence of
886 six earthquake event horizons including the 1939 Erzincan earthquake. Using 18 of the
887 30 radiocarbon-dated samples, a Bayesian ordering-constrained model was used to
888 constrain the age of the six event horizons. The penultimate earthquake (E1) was
889 constrained to A.D. 1408 – A.D. 1804 in trench T3, while data from trench T2 suggest
890 this earthquake occurred after ~A.D. 1660. We correlate this event to the historical A.D.
891 1668 earthquake. The antepenultimate earthquake (E2) was constrained to A.D. 1259 –
892 A.D. 1391 and is correlated to the historical A.D. 1254 earthquake. The fourth
893 earthquake in the sequence (E3) was constrained to A.D. 241 – A.D. 644, which
894 correlates to the historical earthquake in A.D. 499. Event E4 occurred at 881 B.C. – 673

895 B.C. and cannot be matched to a historical earthquake. Event E5, the oldest earthquake
896 recognized at Gunalan, occurred at 1406 B.C. – 1291 B.C., which may correlate to a
897 sequence of earthquakes that may have occurred around 1200 B.C.

898 By comparing the earthquake timing data from this study to the results of other
899 paleoseismic studies on the 1939 Erzincan earthquake rupture segment it appears that this
900 section of the NAF does not always rupture in unison. The A.D. 1668 earthquake seems
901 to have ruptured a western portion of the 1939 rupture segment with the eastern rupture
902 termination being located between Gunalan and the paleoseismic investigation site at
903 Yaylabeli. The A.D. 1254 earthquake seems to have ruptured an eastern portion of the
904 1939 rupture segment with the western termination of the rupture occurring between
905 Resadiye and Gunalan. Earthquakes in A.D. 1045, and A.D. 710 to A.D. 1050 were
906 encountered in paleoseismic investigations to the east of Gunalan. The A.D. 499
907 earthquake was recognized in all of the paleoseismic investigations along the 1939
908 earthquake rupture segment and therefore we tentatively suggest that this earthquake was
909 similar to the 1939 earthquake. An earthquake between 250 B.C. and A.D. 100 was
910 encountered at Resadiye and Cukurcimen, to the west and east of Gunalan, respectively.
911 This may reflect one earthquake that was not evidenced at Gunalan, or it may reflect two
912 separate earthquakes that occurred within a period of several hundred years. An
913 earthquake that occurred around 900 B.C. to 700 B.C. appears to have ruptured most if
914 not all of the 1939 Erzincan earthquake fault rupture segment, like the A.D. 499 event.
915 An earthquake around 1200 B.C. may have had a similar rupture pattern as the A.D. 1254
916 earthquake.

917 The pattern of earthquakes revealed by comparing paleoseismic investigation data along
918 the 1939 Erzincan earthquake rupture segment indicates that it does not behave the same
919 during every seismic cycle, which results in earthquakes of different but still large
920 magnitudes. The time-variable fault rupture lengths are likely to be due to contagion
921 which may come from one or more sources.

922 **Acknowledgements**

923 We acknowledge the European Commission for funding this project as part of the Marie
924 Curie Excellence Grant Project “Understanding the irregularity of seismic cycles: A case
925 study in Turkey” (MEXT-CT-2005-025617: Seismic Cycles). We would like to thank
926 the local people and authorities of the Golova area for their hospitality and allowing us to
927 conduct our investigations. We would like to thank the people of Susehri, where we
928 stayed during field work, for their kind hospitality, especially Jabba who showed us great
929 friendship. Thanks to C. Ballard for reviewing this manuscript and providing useful
930 comments.

931 **References**

932 Ambraseys, N. N., (1970) Some characteristic features of the Anatolian fault zone,
933 *Tectonophysics*, 9, 143-165.

934 Ambraseys, N. N., and C. F. Finkel (1995) *The Seismicity of Turkey and Adjacent Areas:*
935 *A Historical Review, 1500-1800*, 240 pp, Muhittin Salih Eren, Istanbul.

936 Ambraseys, N. N., and J. Jackson (1998) Faulting associated with historical and recent
937 earthquakes in the Eastern Mediterranean region, *Geophysical Journal*
938 *International*, 133, 390-406.

939 Anderson, J.G., S.G. Wesnousky, and M.W. Stirling (1996) Earthquake size as a function
940 of fault slip rate, *Bulletin of the Seismological Society of America*, 86, 683-690.

941 Armijo, R., B. Meyer, A. Hubert, and A. Barka (1999) Westward propagation of the
942 North Anatolian fault into the northern Aegean: timing and kinematics, *Geology*,
943 27, 267-270.

944 Barka, A. (1996) Slip distribution along the North Anatolian fault associated with the
945 large earthquakes of the period 1939 to 1967, *Bulletin of the Seismological*
946 *Society of America*, 86, 1238-1254.

947 Barka, A., H. Akyuz, E. Altunel, G. Sunal, Z. Cakir, A. Dikbas, B. Yerli, R. Armijo, B.
948 Meyer, and J. de Chabaliere (2002) The Surface Rupture and Slip Distribution of
949 the 17 August 1999 Izmit Earthquake (M 7.4), North Anatolian Fault, *Bulletin of*
950 *the Seismological Society of America*, 92, 43-60.

- 951 Barka, A. A. (1992) The North Anatolian fault zone, *Annales Tectonicae*, 6, 164–195.
- 952 Barka, A. A., S. H. Akyuz, H. A. Cohen, and F. Watchorn (2000) Tectonic evolution of
953 the Nixsar and Tasova-Erbaa pull-apart basins, North Anatolian Fault Zone: their
954 significance for the motion of the Anatolian block, *Tectonophysics*, 322, 243-264.
- 955 Biasi, G., and R. Weldon (1994) Quantitative refinement of calibrated C-14 distributions,
956 *Quaternary Research*, 41, 1–18.
- 957 Biasi, G. P., R. J. Weldon, T. E. Fumal, and G. G. Seitz (2002) Paleoseismic event dating
958 and the conditional probability of large earthquakes on the southern San Andreas
959 Fault, California, *Bulletin of the Seismological Society of America*, 92, 2761-2781.
- 960 Bronk Ramsey, C. (2007) OxCal Program v. 4.0.5, Radiocarbon Accelerator unit,
961 University of Oxford, UK. <https://c14.arch.ox.ac.uk/oxcal.html>
- 962 Dolan, J., F. D. Bowman, and C. Sammis (2007) Long range and long-term fault
963 interactions in southern California, *Geology*, 35(9), 855–858,
964 doi:10.1130/G23789A.1.
- 965 Flerit, F., R. Armijo, G. King, and B. Meyer (2004) The mechanical interaction between
966 the propagating North Anatolian Fault and the back-arc extension in the Aegean,
967 *Earth and Planetary Science Letters*, 224, 347-362. doi:
968 10.1016/j.epsl.2004.05.028
- 969 Fraser, J. G., J. S. Pigati, A. Hubert-Ferrari, K. Vanneste, U. Avsar, and S. Altinok
970 (2009a) A 3000-year record of ground-rupturing earthquakes along the central
971 North Anatolian Fault near Lake Ladik, Turkey, *Bulletin of the Seismological
972 Society of America*, 99, doi:10.1785/0120080024
- 973 Fraser, J. G. (2009b) Four new paleoseismic investigations on the North Anatolian Fault,
974 Turkey, in the context of existing data, Ph.D. thesis, 284 pp, Univ. Libre de
975 Bruxelles, Belgium, Brussels.
- 976 Fraser, J. G., K. Vanneste, A. Hubert-Ferrari (2010a) Recent behavior of the North
977 Anatolian Fault: Insights from an integrated paleoseismological data set, *Journal
978 Of Geophysical Research*, 115, B09316, doi:10.1029/2009JB006982, 2010
- 979 Fraser, J. G., A. Hubert-Ferrari, K. Vanneste, S. Altinok, and L. Drab (2010b) A relict
980 sedimentary record of seven earthquakes between 600 AD and 2000 BC on the
981 central North Anatolian Fault at Elmacik, near Osmaniye, Turkey, *Geol. Soc. Am.
982 Bull.*, 122, p. 1830–1845, doi: 10.1130/B30081.1

- 983 Guidoboni, E., and A. Comastri (Eds) (2005) *Catalogue of earthquakes and tsunamis in*
984 *the mediterranean area from the 11th to the 15th century*, 1037 pp, Istituto
985 Nazionale de Geophysical e Vulcanologia, Bologna.
- 986 Guidoboni, E., A. Comastri, and G. Traina (1994) *Catalogue of ancient earthquakes in*
987 *the Mediterranean area up to the 10th century*, 504 pp. Istituto Nazionale di
988 Geofisica, Rome.
- 989 Gulen, L., A. Pinar, D. Kalafat, N. Ozel, G. Horasan, and M. Yilmazer (2002) Surface
990 Fault Breaks, Aftershock Distribution, and Rupture Process of the 17 August 1999
991 Izmit, Turkey, Earthquake, *Bulletin of the Seismological Society of America*, 92,
992 230-244.
- 993 Hartleb, R. D., J. F. Dolan, H. S. Akyuz, and B. Yerli (2003) A 2000-Year-Long
994 Paleoseismologic Record of Earthquakes along the Central North Anatolian Fault,
995 from Trenches at Alayurt, Turkey, *Bulletin of the Seismological Society of*
996 *America*, 93, 1935-1954.
- 997 Hartleb, R. D., J.F. Dolan, O. Kozaci, H. S. Akyuz, and G. G. Seitz (2006) A 2500-yr-
998 long paleoseismologic record of large, infrequent earthquakes on the North
999 Anatolian fault at Cukurcimen, Turkey, *Bulletin of the Geological Society of*
1000 *America*, 118, 823-840. doi: 10.1130/B25838.1
- 1001 Hilley, G. E., and J. J. Young (2008a) Deducing Paleoearthquake Timing and Recurrence
1002 from Paleoseismic Data, Part I: Evaluation of New Bayesian Markov-Chain
1003 Monte Carlo Simulation Methods Applied to Excavations with Continuous Peat
1004 Growth, *Bulletin of the Seismological Society of America*, 98, doi:
1005 10.1785/0120020077
- 1006 Hilley, G. E., and J. J. Young (2008b) Deducing Paleoearthquake Timing and Recurrence
1007 from Paleoseismic Data, Part II: Analysis of Paleoseismic Excavation Data and
1008 Earthquake Behavior along the Central and Southern San Andreas Fault, *Bulletin*
1009 *of the Seismological Society of America*, 98, doi: 10.1785/0120070012
- 1010 Hubert-Ferrari, A., R. Armijo, G. King, B. Meyer, and A. Barka (2002) Morphology,
1011 displacement, and slip rates along the North Anatolian Fault, Turkey, *Journal of*
1012 *Geophysical Research*, 107, doi: 10.1029/2001JB000393.
- 1013 Hubert-Ferrari, A., G. King, J. Van der Woerd, I. Villa, E. Altunel, and E. Armijo (2009)
1014 Long-term evolution of the North Anatolian Fault: new constraints from its
1015 eastern termination, *Collision and Collapse at the Africa–Arabia–Eurasia*
1016 *Subduction Zone* The Geological Society, London, Special Publications, vol. 311,
1017 edited by D.J.J. Van Hinsbergen, M.A. Edwards, and R. Govers pp. 133-154, doi:
1018 10.1144/SP311.5, The Geological Society London.

- 1019 Keefer, D. K. (1984) Landslides caused by earthquakes, *Bulletin of the Geological*
1020 *Society of America*, 95, 406-421.
- 1021 Kocyigit, A. (1989) Susehri basin: an active fault-wedge basin on the North Anatolian
1022 Fault Zone, Turkey, *Tectonophysics*, 167, 13-29.
- 1023 Kocyigit, A. (1990) Tectonic setting of the Golova basin: Total offset of the North
1024 Anatolian Fault zone, E Pontide, Turkey, *Annales Tectonicae*, 2, 155–170.
- 1025 Kozaci, O., J. F. Dolan, O. Yonlu, and R. D. Hartleb (2011) Paleoseismologic evidence
1026 for the relatively regular recurrence of infrequent, large-magnitude earthquakes on
1027 the eastern North Anatolian fault at Yaylabeli, Turkey, *Lithosphere*, 3, 37-54, doi:
1028 doi: 10.1130/L118.1.
- 1029 Lienkaemper, J. J., and C. Bronk Ramey (2009) OxCal: Versatile tool for developing
1030 paleoearthquake chronologies – a primer, *Seismological Research Letters*, 80,
1031 431-434, doi: 10.1785/gssrl.80.3.431
- 1032 Nur, A., and E. H. Cline (2000) Poseidon's horses: Plate tectonics and earthquake storms
1033 in the Late Bronze Age Aegean and Eastern Mediterranean, *Journal of*
1034 *Archaeological Science*, 27, 43-63.
- 1035 Okumura, K., T. Yoshioka, and I. Kusu (1994) Surface faulting on the North Anatolian
1036 Fault in these two millennia, Proceedings of the workshop on paleoseismology,
1037 *Open-File Report 94-568*, pp. 143-144, USGS, Menlo Park, California.
- 1038 Perkins, D. M. (1987) Contagious fault rupture, probabilistic hazard, and contagion
1039 observability. In: Crone A J, Omdahl E M (eds). Conference proceedings:
1040 Directions in Paleoseismology, US Geol. Surv., Open file report 87-673, 428 -
1041 439
- 1042 Pondard, N., R. Armijo, G. C. P. King, B. Meyer, and F. Flerit (2007) Fault interactions
1043 in the Sea of Marmara pull-apart (North Anatolian Fault): earthquake clustering
1044 and propagating earthquake sequences, *Geophysical Journal International*, 171,
1045 1185-1197. doi: 10.1111/j.1365-246x.2007.03580.x
- 1046 Reilinger, R., S. McClusky, P. Vernant, S. Lawrence, S. Ergintav, R. Cakmak, H. Ozener,
1047 F. Kadirov, I. Guliev, R. Stepanyan, M. Nadariya, G. Hahubia, S. Mahmoud, K.
1048 Sakr, A. ArRajehi, D. Paradissis, A. Al-Aydrus, M. Prilepin, T. Guseva, E. Evren,
1049 A. Dmitrotsa, S. V. Filikov, F. Gomez, R. Al-Ghazzi, and G. Karam (2006) GPS
1050 constraints on continental deformation in the Africa-Arabia-Eurasia continental
1051 collision zone and implications for the dynamics of plate interactions, *Journal of*
1052 *Geophysical Research*, 111, doi: 10.1029/2005JB004051

- 1053 Reimer, P. J., M. G. L. Baillie, E. Bard, A. Bayliss, J. W. Beck, C. J. H. Bertrand, P. G.
 1054 Blackwell, C. E. Buck, G. S. Burr, K. B. Cutler, P. E. Damon, R. L. Edwards, R.
 1055 G. Fairbanks, M. Friedrich, T. P. Guilderson, A. G. Hogg, K. A. Hughen, B.
 1056 Kromer, F. G. McCormack, S. W. Manning, C. B. Ramsey, R. W. Reimer, S.
 1057 Remmele, J. R. Southon, M. Stuiver, S. Talamo, F. W. Taylor, J. Van Der Plicht,
 1058 and C. E. Weyhenmeyer (2004) IntCal04 terrestrial radiocarbon age calibration,
 1059 0-26 Ka cal BP, *Radiocarbon*, 46, 1029-1058.
- 1060 Sieh, K. (1996) The repetition of large earthquake ruptures, *Proc. Natl. Acad. Sci. U. S.*
 1061 *A.*, 93, 3764–3771, doi:10.1073/pnas.93.9.3764.
- 1062 Sengor, A., O. Tuysuz, C. Imren, M. Sakinc, H. Eyidogan, N. Gorur, X. Le Pichon, and
 1063 C. Rangin (2005) The North Anatolian Fault: A New Look, *Annual Review of*
 1064 *Earth and Planetary Sciences*, 33, 37-112, doi:
 1065 10.1146/annurev.earth.32.101802.120415.
- 1066 Sengor, A. M. C., N. Gorur, and F. Saroglu (1985) Strike-slip faulting and related basin
 1067 formation in zones of tectonic escape: Turkey as a case study, *Strike-slip faulting*
 1068 *and basin formation*, Society of Economic Paleontologists and Mineralogists
 1069 Special Publication No. 37, edited by: Biddle, K.T., and N. Christie-Blick, pp.
 1070 227-264, Society of Economic Paleontologists and Mineralogists, Tulsa,
 1071 Oklahoma.
- 1072 Stein, R. S., A. A. Barka, and J. H. Dieterich (1997) Progressive failure on the North
 1073 Anatolian fault since 1939 by earthquake stress triggering, *Geophysical journal*
 1074 *international*, 128, 594–604.
- 1075 Stuiver, M. and H. A. Polach (1977) Reporting of 14C Data, *Radiocarbon*, 19, 355–363.
- 1076 Wells, D. L., and K. J. Coppersmith (1994) New empirical relationships among
 1077 magnitude, rupture length, rupture width, rupture area, and surface displacement,
 1078 *Bulletin of the Seismological Society of America*, 84, 974-1002
- 1079 Wesnousky, S. G. (2006) Predicting the endpoints of earthquake ruptures, *Nature*, 444,
 1080 358–360, doi:10.1038/nature05275.
- 1081 Zabci, C., V. Karabacak, T. Sancar, H.S. Akyuz, E. Altunel, H. Gursoy, and O. Tatar
 1082 (2008) The possible eastward continuation of the 17 August 1668 Anatolian
 1083 Earthquake on the North Anatolian Fault (NAF), Turkey, *Geophysical research*
 1084 *Abstracts*, 10, abstract 05542.

1085 **ANNEX A – Stratigraphic Unit Descriptions**

1086

Symbol	Unit Descriptions
Topsoil	Brown sandy SILT with high organic content.
S1	Grey SAND and silty SAND planar and cross bedded laminated in places. Contains some thin pebbly horizons particularly near the base.
S2	Grey silty SAND finely laminated with cross bedding.
S3	Undifferentiated S2 and S4.
S4	Beige silty SAND, clayey at some points.
C1	Beige silty CLAY.
Ps1	Dark brown SILT. Buried A horizon – Paleosol.
C2	Beige silty CLAY.
F1	Brown clayey SILT. Lower boundary with F2 is gradational.
F2	Grey gravelly silty CLAY. Upper boundary with F1 is gradational.
Ps2	Dark brown SILT. Buried A horizon – Paleosol. On the east wall this unit has a lens of unit3 around which it grades laterally into unit C4.
C3	Light brown silty gravelly CLAY.
C4	Brown CLAY. Not present on the west wall. Probably altered Ps2 due to interaction with the water table.
C5	Light brown CLAY with occasional gravel clasts. Grades into blue grey CLAY to the south on the east wall – probably due to interaction with the water table.
Ps3	Dark brown SILT. Buried A horizon – Paleosol.
C6	Light brown CLAY with occasional gravel clasts, contains more gravel near the fault. Only present north of the fault zone on the east wall.
C7	Light brown CLAY. Only present north of the fault zone on the east wall.
Gx1	Beige clayey GRAVEL.
Gx2	Grey GRAVEL with clay coating – no matrix.
Gx3	Grey sandy GRAVEL with some imbrication.
Fz	Shear zone mixed materials with a fabric semi parallel to adjacent fault(s).
Cx	Light Brown CLAY – This generic label has been generated as we do not know which clay rich unit this correlates to.

1087 **Table A.A-1.** Paleoseismic trench T1 trench log stratigraphic unit descriptions. Symbols
 1088 are used on Figures 3 and 4.

1089

1090

Symbol	Unit Descriptions
Topsoil	Brown sandy SILT with high organic content.
S1	Brownish grey, silty SAND
S2	Pale brown silty fine SAND. In and north of the fault zone contains some gravel layers.
S3	Undifferentiated S2 and S4
S4	Greyish brown silty fine SAND
S5	Undifferentiated S2, S4, and S6
S6	Pale brown silty fine SAND
S7	Greyish brown silty fine SAND
S8	Pale yellowish brown, silty fine SAND. Near horizontal 13 contains some lenses of coarse sand. In and north of the fault zone contains some gravel layers.
I1	Pale brown laminated SAND. Not present on the east wall.
I2	Pale brown silty CLAY. Not present on the east wall.
I3 (g)	This unit is comprised of material similar to unit s8 in the upper half and a mixture of unit Ps1, Ps2 and S8 in the bottom half. 2 of the subunits in this infill, denoted with a "g" contain abundant gastropod fragments. Not present on the west wall.
G1	Grey brown, silty sandy GRAVEL. In some places this unit is bedded with gravel rich beds in others it is well mixed.
Ps1a	Purple brown SILT. A buried A horizon – Paleosol.
G2	Grey brown, silty sandy GRAVEL. Very localized and only present on the east wall.
Ps1b	Grayish brown silty SAND with some oxide nodules. A buried B horizon – Paleosol. On Both walls, in the fault zone and north of the fault zone the lower part of this unit has obvious liquefaction features and much of this unit may owe its origin to this source. It is unlikely that there was co-seismic sedimentation that was not associated to the earthquake.
Ps2a	Red brown gravelly sandy clayey SILT with some gravel.PS2# denotes 3 interesting features. The top area is disturbed and slightly darker. The middle area is rich in oxide nodules. The bottom area is silty sand. These 3 features seem to be related to bioturbation.
Ps2b	Brown silty sand GRAVEL.
S9	Greenish Brown Silty SAND.
S10	Brown silty fine SAND.
S11	Grayish brown, clayey medium SAND.
S12	Brown clayey silty fine SAND.
F1	Brown silty CLAY. More greenish brown on the east wall. F1# denotes 3 lenses within unit F1. The northern lens is comprised of coarse SAND, and the middle and southern lens are fine sand.
F2	Blue grey CLAY.
F3	Light reddish brown Sand SILT. More light brown on the east wall.
G3	Grey brown silty GRAVEL. Not present of the west wall.
L1	Graying brown pebbly silty SAND. (liquefaction deposit)
L2	Grayish brown silty pebbly SAND. (liquefaction deposit)

1092
1093
1094
1095

Table A.A-2. Paleoseismic trench T2 trench log stratigraphic unit descriptions. Symbols are used on Figures 5 and 6.

Symbol	Description
<i>South of the fault</i>	
Topsoil	Dark brown SILT with some pebbles – gravels.
W1	Brown gravelly pebbly SILT grading upwards into silty pebbly GRAVEL, grain sizes vary N-S within unit.
S1	Orange brown fine SAND, thin and discontinuous on the east wall.
W2	Dark brown silty GRAVEL, not recognized on the east wall. Becomes less gravelly away from the fault.
Ps1	Dark grey SILT, columnar soil structure, Paleosol.
F1	Dark red brown, silty CLAY, columnar soil structure, not recognized on the west wall. Buried C horizon.
S2	Pale brown silty SAND with some laminations and a blocky soil structure. Becomes more silty and has a columnar structure near the fault. Upper limit is generally gradational on the west wall and sharp on the east wall.
Ps2	Pale brown gravelly (mainly at base of unit) SILT.
W3	Grey silty GRAVEL, becomes less gravelly towards the fault zone and becomes more red brown and less gravelly south of a horizontal distance of 9m. Upper contacts with unit Ps2 and lower contacts with unit F2 are gradational. On the east wall the contacts with overlying unit Ps2 and underlying F2 are gradational and subtle. On the west wall these units can only be clearly distinguished north of a horizontal distance of 10m, to the south there is only a subtle and vertically streaked color change – pale brown at the top and the bottom with a band of red brown (W3?).
	Pale brown SILT.
W4a	Brown sandy PEBBLES, not recognized on the west wall.
W4b	Brown silty PEBBLES, not recognized on the west wall.
W4c	Brown Cobbly SILT/ silty COBBLES with some sand. There is less coarse materials south of a horizontal distance of 9m. South of a horizontal distance of 10m on the east wall, the unit becomes red brown pebbly clayey SILT. South of a horizontal distance of 10m on the west wall and a horizontal distance of 12m on the east wall this unit is indistinguishable from the underlying unit F3a and is described as F3b.
F3a	Brown silty PEBBLES grading horizontally to SILT with some pebbles.
F3b	Brown clayey silty PEBBLES with some cobbles.
F3/4u	This unit is used to describe an area of strata where we could not recognize continuous units. Generally there is some colour variation between pale brown and red brown but it is vertically streaked in “flame like” structures which we attribute to dense plant roots probably associated with a phase of wet-land vegetation e.g. reeds.
W5a	Brown pebbly silty COBBLES, not recognized on the west wall.
W5b	Red brown silty GRAVEL.
F4a	Brown (pale brown grading upwards to red brown at the southern end of the trench) clayey SILT with some gravel, south of a horizontal distance of 9m this unit is vertically streaked with red brown.
F4b	Greenish grey (pale brown towards base at the southern end of the trench) silty CLAY. The upper contact of this unit with F4a and the lower contact of unit F4b, with unit F5 is vertically streaked.
S3	Pale brown silty SAND. This unit is mostly very thin and is not present south of a horizontal distance of 9.5m this unit was not recognized on the east wall.
W6	Brown sandy pebbly silty GRAVEL with some cobbles. Between the horizontal distances of 9m and 10m the percentage of coarse clasts decreases from the dominant fraction to nearly absent, therefore unit W6 grades horizontally into unit F5.

F5	Grey brown SILT with some pebbles.
F6a	Pale brown silty CLAY. Grades to the south into unit F6c. Not recognized on the east wall.
F6b	Light pale brown silty CLAY with some sand. Grades to the south into unit F6c. Not recognized on the east wall.
F6c	Red brown near the top of the unit grading down to pale brown clayey SILT, abundant vertical color streaking.
S4	Grey brown fine-medium SAND.
W7a	Grey Brown Sandy PEBBLES/Pebbly SAND.
W7b	Grey Brown Sandy PEBBLES/Pebbly SAND.
F7	Red brown CLAY, grading down into pale brown SILT, grading down into pale brown sandy SILT with some cobbles distributed along the base of the unit.
S5	Grey brown fine-medium SAND.
F8	Brown and grey brown CLAY.
Ga/F8	Gradational transition between units Ga and F8.
S6	Grey brown fine SAND, this unit is seldom thicker than 5mm. Not exposed on the west wall.
F9	Brown and grey brown CLAY. Not exposed on the west wall.
Ga/F9	Gradational transition between units Ga and F9. Not exposed on the west wall.
Ga	Brown silty GRAVEL and gravelly SILT (varies chaotically) with increased cobble content along the top of this unit.
<i>North of the southernmost fault</i>	
UG	Undifferentiated gravel – Brown silty GRAVEL/ Gravelly SILT. Structure, including package boundaries, destroyed by burrowing animals and to a lesser degree vegetation. Equivalent to units G1 – 13 which are generally hard to trace.
G1	Grey silty GRAVEL.
G2	Undifferentiated G1 and G3.
G3	Grey brown gravelly silty PEBBLES.
G4	Grey brown PEBBLES clast supported (no matrix) with some cobbles in the southern half of the unit.
G5	Undifferentiated G4 and G6.
G6	Grey brown PEBBLES clast supported with some silt matrix.
G7	Brown silty GRAVEL clast supported.
G8	Undifferentiated G7 and G9.
G9	Brown silty gravelly COBBLES clast supported
G10	Grey brown silty pebbly GRAVEL
G11	Brown silty GRAVEL
G12	Grey brown (grey mottled brown in some places) silty sandy GRAVEL. Not present on the east wall.
G13	Brown silty PEBBLES, horizontally imbricated. This is interpreted as an fissure-infill deposit. Not present on the east wall.
Rg1	Illuviated river gravel (see the unit description for Rg). Grey brown (grey mottled brown in some places) silty sandy GRAVEL.
Rg	River Gravel, grey sandy GRAVEL, weakly defined bedding strongly deformed (generally tilting down to the South), many clasts have carbonate coatings on their bottom half, near faults clasts are aligned (near vertical) with their coatings also rotated. We correlate this unit to "Pliocene continental clastics (Cobanlı group)" which form the scarp to the north of the trench (Kocçigit, 1990 pg.157).

1097
1098

Table A.A-3. Paleoseismic trench T3 trench log stratigraphic unit descriptions. Symbols are used on Figures 7 and 8.

1099 **ANNEX B – Detailed Radiocarbon Dating Information**

1100 **Bulk Sample Processing**

1101 A 60 g sub-sample was selected from the bulk sample. The samples were split into two
1102 30g samples and the following procedures were applied. Samples were submerged in
1103 hydrochloric acid (40% HCl) for 24 hours to remove carbonates. Then the samples were
1104 placed in hydrofluoric acid (40% HF) for 12 hours and continuously agitated, and then
1105 they rested in stronger hydrofluoric acid (70% HF) for 7 days to remove silicates. The
1106 samples were then treated with potassium hydroxide (10% KOH) for 15 minutes and with
1107 hot hydrochloric acid (10% HCl) for 5 minutes to remove humic acid as well as
1108 additional unwanted organic and inorganic residues. The samples were then sieved and
1109 the 10 – 63 micrometer fraction of the samples were treated with hot hydrochloric acid
1110 (10% HCl) for 5 minutes. They were then washed, dried, the samples were recombined
1111 (i.e. the two portions of the sample) and were submitted to the radiocarbon dating
1112 laboratory where no further chemical pretreatments were administered.

Trench	Event Horizon	Sample #	Soil unit	Trench wall	Lab Number (Aeon:)	Material	Yield (%)	Mass (mg) (3 d.p.)	d13C (vpdp) (3d.p.)	FMC (4.d.p.)	FMC uncertainty	Unrounded CRA (yrsBP) (2.d.p)		Rounded CRA (yrsBP)		Calibrated age	Order constrained calibrated age		
													±		±				
Trench 1	<i>T1E1</i>	37	C4	E	139	C	49.2	1.198	-26.360	0.9671	0.0041	268.55	33.57	270	35	A.D. 1494–1951	not modelled		
		<i>T2E0 and T2E1</i>																	
Trench 2		42	Ps1a	W	215	C	51.8	1.184	-27.579	0.9801	0.0041	161.70	33.73	160	35	A.D. 1663–1953	not modelled		
		41	Ps1a	W	141	C	56.9	1.034	-24.485	0.9790	0.0039	170.39	32.11	170	35	A.D. 1657–1953	not modelled		
		40	Ps1b	W	140	C	28.6	1.289	-27.896	0.0193	0.0003	31723.31	109.12	31700	150	29995–29559 B.C.	not modelled		
		47	Ps1b	E	217	C	3.3	1.286	-27.871	0.8434	0.0033	1367.94	31.44	1370	40	A.D. 608–761	not modelled		
		50	S9	E	218	C	59.6	1.304	-27.205	0.9586	0.0040	339.23	33.50	340	35	A.D. 1468–1641	not modelled		
		<i>T2E2</i>																	
		43	Ps2	W	216	C	59.7	1.257	-26.490	0.8044	0.0049	1748.66	49.02	1750	50	A.D. 137–402	not modelled		
		49	Ps3	W	142	C	44.3	1.099	-24.395	0.8069	0.0033	1723.06	32.69	1720	40	A.D. 242–399	not modelled		
Trench 3		26	W2	W	134	C	5.3	1.055	-22.295	0.9158	0.0040	706.84	35.04	710	40	A.D. 1227–1388	reworked		
		<i>T3E0</i>																	
		2	F1	E	130	C	57.2	1.138	-23.322	0.9930	0.0040	56.58	32.34	60	35	A.D. 1693–modern	A.D. 1706–1926		
		B51	Ps2	E	266	B	26.6	1.109	-26.466	0.9816	0.0047	149.38	38.42	150	40	A.D. 1666–1953	A.D. 1666–1888		
		B53	F2	E	262	B	36.5	1.102	-24.209	0.9286	0.0036	595.31	31.13	600	35	A.D. 1297–1411	reworked		
		<i>T3E1</i>																	
		27	F3b	W	136	C	18.2	1.140	-24.099	0.9338	0.0037	549.92	31.39	550	35	A.D. 1311–1434	A.D. 1337–1440		
		B54	W4c	E	263	B	25.0	1.319	-24.525	0.9357	0.0038	534.20	32.96	530	35	A.D. 1317–1440	A.D. 1324–1428		
		6	W4c	E	132	C	50.6	1.056	-22.888	0.9318	0.0036	567.37	31.36	570	35	A.D. 1304–1425	A.D. 1305–1413		

<i>T3E2</i>																
	B55	F3a	E	281	B	12.8	1.163	-28.100	0.9069	0.0035	785.03	30.59	790	35	A.D. 1190–1281	A.D. 1189–1280
	5	F3a	E	131	C	28.7	0.648	-25.900	0.9128	0.0035	733.25	31.06	730	35	A.D. 1222–1296	A.D. 1224–1291
	B57	F3a	E	282	B	12.0	1.114	-28.700	0.8842	0.0033	988.21	30.35	990	35	A.D. 989–1154	A.D. 989–1153
	28	F3/4u	W	227	C	3.2	1.272	-26.176	0.6778	0.0025	3123.95	29.00	3120	30	1490–1314 B.C.	reworked
	B60	W5b	E	283	B	6.9	0.867	-27.900	0.8391	0.0038	1409.51	35.84	1410	40	A.D. 576–667	A.D. 578–669
<i>T3E3</i>																
	B61	F4a	E	284	B	11.6	1.032	-29.300	0.8027	0.0039	1765.76	39.00	1770	40	A.D. 136–381	A.D. 133–379
	B64	F4b	E	285	B	7.0	1.185	-29.500	0.7458	0.0030	2356.06	32.05	2360	40	536–380 B.C.	reworked
	25	F4b	W	226	C	2.3	0.808	-26.841	0.6207	0.0026	3830.38	33.80	3830	40	2458–2150 B.C.	reworked
	24	F4b	W	225	C	7.0	0.672	-27.627	0.7662	0.0029	2139.63	30.27	2140	40	353–55 B.C.	338–52 B.C.
	23	F5	W	224	C	10.0	0.699	(-25)	0.7653	0.0041	2148.84	43.23	2150	50	359–54 B.C.	363–122 B.C.
	B68	F5	E	287	B	11.3	0.984	-29.500	0.7238	0.0026	2596.71	28.34	2600	30	815–672 B.C.	811–568 B.C.
	33	W6	W	137	C	33.5	1.248	-25.119	0.7892	0.0029	1901.40	29.09	1900	30	A.D. 27–213	too young
<i>T3E4</i>																
	12	F6c	E	220	C	4.0	1.064	-28.047	0.5882	0.0021	4262.80	27.99	4260	30	2919–2779 B.C.	reworked
	16	F6c	W	221	C	23.1	1.351	-27.085	0.7975	0.0035	1817.79	35.59	1820	40	A.D. 86–323	too young
	B70	F6c	E	264	B	26.6	1.330	-24.450	0.7203	0.0028	2635.86	31.49	2640	40	890–774 B.C.	897–789 B.C.
	10	F6c	E	236	C	2.4	1.002	-25.729	0.5935	0.0022	4190.86	29.37	4190	30	2889–2676 B.C.	reworked
	B71	F6c	E	261	B	17.9	1.115	-24.186	0.6854	0.0023	3033.88	27.11	3030	30	1394–1213 B.C.	1359–1134 B.C.
	17	F6c	W	222	C	9.6	0.981	-26.671	0.6870	0.0032	3015.41	37.18	3020	40	1390–1130 B.C.	1347–1127 B.C.
	34	F6b	W	138	C	22.7	1.154	-22.9292	0.8120	0.0031	1672.71	30.98	1670	40	A.D. 258–429	too young
	B72	S4	E	267	B	3.9	0.401	(-25)	0.6829	0.0029	3064.06	33.86	3060	40	1417–1220 B.C.	1381–1266 B.C.
<i>T3E5</i>																
	B73	F7	E	265	B	15.0	1.083	-23.746	0.6640	0.0022	3289.49	26.95	3290	30	1628–1500 B.C.	reworked
	9	F8	E	133	C	48.3	0.628	-31.200	0.8193	0.0039	1601.24	37.81	1600	40	A.D. 385–553	too young
	B81	F9	E	286	B	37.7	0.887	-29.200	0.6822	0.0023	3071.52	27.22	3070	30	1413–1268 B.C.	1420–1321 B.C.

1114 **Table A.B-1.** Radiocarbon dating data from paleoseismic investigations at Gunalan. See text and figures for description of event horizons. ‘Lab-number’ is the unique
1115 identifier for each radiocarbon analysis performed by Aeon. In the ‘Material’ column ‘C’ stands for charcoal and ‘B’ stands for bulk sample. ‘Yield’ is the
1116 percentage of carbon in the subsample analyzed. ‘Mass’ is the mass of the carbon subjected to AMS measurement and does not include the portion used for stable
1117 isotope measurement. ‘ $\delta^{13}C$ ’ is the difference between the $^{13}C/^{12}C$ ratio of the sample and that of the VPDB standard, expressed in per mille, values in brackets are
1118 estimated. ‘FMC’ is the ^{14}C activity ratio, which is corrected for isotopic fractionation and background activity. ‘CRA’ is the conventional radiocarbon age,
1119 normalized to -25 based on a 5568-year half-life. All ages are given at the maximum (Max) or minimum (Min) of the 2σ age range.

1120 **Figure Captions**

1121 **Figure 1. a.)** Map of the Anatolian plate region. Heavy black arrows show the direction
1122 of plate motion based on GPS studies (relative to a fixed Eurasia), with the velocity in
1123 mm/yr shown in brackets (Reilinger et al., 2006). Red lines depict present plate boundary
1124 faults, and black lines are important faults. DSF, Dead Sea fault; NAF, North Anatolian
1125 Fault; EAF, East Anatolian fault; NEAF, Northeast Anatolian fault; MCT, Main
1126 Caucasus thrust; AR, Alborz Range; CB, Caucasus Block; CF, Chalderan Fault; TF,
1127 Tabriz Fault; AsF, Ashgabat Fault; PSSF, Pembak-Sevan-Sunik Fault; and OF, Ovacik
1128 fault. (modified from *Fraser et al. 2010a*). **b.)** Map of 20th century earthquake ruptures
1129 near Gunalan (location of map shown by rectangle labelled ‘box b’ in Fig. 1a).
1130 Paleoseismic trench locations are shown with stars (this study white, other studies black),
1131 and filled circles show selected major settlements. Significant pull-apart basins are
1132 numbered: 1) Tasova-Erbaa pull-apart basin, 2) Niksar pull-apart basin and 3) Erzincan
1133 pull-apart basin. Significant fault splays are labelled: EF, Ezinepazari fault; AIF, Almus
1134 fault; and OF, Ovacik fault. **c.)** Fault segments and right-lateral displacements associated
1135 with the 1939 Erzincan earthquake (modified from *Barka, 1996* see references therein).
1136 The irrigation canal offset by 5.6m ~2.5km west of Gunalan (Fig. 2a) (*Kocyigit, 1990, pg*
1137 *165*) is included in *Barka’s (1996)* plot and indicated with an arrow.

1138 **Figure 2. a.)** Fault map of the study area draped over a satellite image with key features
1139 highlighted. **b. and c.)** Geomorphic maps of areas near paleoseismic trenches. **d.)** A
1140 photo showing faults C and A, **e.)** A photo showing faults A and B and the depression in
1141 between. **f.)** A photo showing the lateral spread the structure of which is depicted in box
1142 c. The location and orientation of the photos in Fig. 2 d, e, and f is shown in Fig2a.

1143 **Figure 3. a)** Trench log of paleosesimic trench T1. The horizontal and vertical axes are
1144 labeled in meters. **b)** Legend for box a. Unit symbols correlate to stratigraphic
1145 descriptions that are presented in Table A.A-1 (Annex A). See Figure 4 for a photo
1146 mosaic of a section of the east wall.

1147 **Figure 4.** Photo mosaic of a section of the east wall of paleoseismic trench T1. The
1148 horizontal and vertical axes are labeled in meters. Unit symbols correlate to stratigraphic
1149 descriptions that are presented in Table A.A-1 (Annex A). See Fig. 3 for legend.

1150 **Figure 5. a)** Trench log of paleoseismic trench T2. The horizontal and vertical axes are
1151 labeled in meters. **b)** Legend for box a. Unit symbols correlate to stratigraphic
1152 descriptions that are presented in Table A.A-2 (Annex A).

1153 **Figure 6.** Photo mosaic of paleoseismic trench T2 overlain by the lines and unit labels of
1154 the trench log for comparison with the trench log (Fig. 5). The horizontal and vertical
1155 axes are labeled in meters. Unit symbols correlate to stratigraphic descriptions that are
1156 presented in Table A.A-2 (Annex A). See Fig. 5 for legend.

1157 **Figure 7. a)** Trench log of paleoseismic trench T3. The horizontal and vertical axes are
1158 labeled in meters. Note that (1) a gap has been plotted between the upper and lower walls
1159 so that the whole logs can be seen, (2) the yellow outline of the sand layers lightly
1160 exaggerates the real thickness of these layers. **b)** Legend for box a. Unit symbols
1161 correlate to stratigraphic descriptions that are presented in Table A.A-3 (Annex A).

1162 **Figure 8.** Photo mosaic of paleoseismic trench T3 overlain by the lines and unit labels of
1163 the trench log for comparison with the trench log (Fig. 7). The horizontal and vertical
1164 axes are labeled in meters. Unit symbols correlate to stratigraphic descriptions that are
1165 presented in Table A.A-3 (Annex A). Note that a gap has been plotted between the upper
1166 and lower walls so that the whole logs can be seen. See Figure 7 for legend.

1167 **Figure 9. a)** Plot of the order-constrained Bayesian model (using OxCal software, Bronk
1168 Ramsey, 2007) constructed for trench T3, showing the calibrated sample age probability
1169 density functions (PDFs) (blue fill, no boundary), modeled sample age PDFs (no fill, red
1170 boundary), and earthquake age PDFs (black filled). Samples grouped into phases in the
1171 order-constrained Bayesian model (electronic supplement 1) are indicated with brackets.
1172 Samples were calibrated using the IntCal04 curve (Reimer *et al.*, 2004). T3E0 was
1173 entered into the model as a fixed date corresponding to the Erzincan rupture in A.D.

1174 1939. **b)** Plot of the PDFs of the inter-event times calculated using OxCal (*Bronk*
1175 *Ramsey, 2007*). PDFs labeled IET_{n-m} correspond to individual inter-event times (i.e.
1176 IET_{0-1} is the inter-event time between event E0 and event E1), SIET is the summed
1177 inter-event time, and RI_{avg} is the average recurrence interval. Black stars show the inter-
1178 event times inferred from the correlated historical earthquakes.

1179 **Figure 10.** Summary plot of along-strike paleoearthquake fault rupture segments
1180 estimated using the timing of earthquakes determined in the different paleoseismic
1181 investigations along the 1939 Erzincan earthquake fault rupture segment. Data for each
1182 of the sites come from: Resadiye, Fraser (2009b); Gunalan, this study; Yaylabeli, Kozaci
1183 et al. (2011); and Cukurcimen, *Hartleb et al.* (2006);

1184

Year	Ref.	X	Comment
A.D. 1919	a	A	Reported ~50km north of Resadiye.
A.D. 1754	b	B	Reported in Sivas.
A.D. 1684	b	A	Reported from Amasaya – refers to Niksar.
A.D. 1668	a,b,c	D	Reported widely in northern Turkey. Probably reflects more than one earthquake closely spaced in this year.
A.D. 1583	a	D	Extensive destruction in Erzincan.
A.D. 1579	b,c	B	Damage reported in Corum, Amasaya, and Erzincan Regions – may have been 2 separate events.
A.D. 1575	b	A	Reported 5 November in Erzincan. Probably a localized earthquake.
A.D. 1543	b	B/C	Reported 4 April Corum, Tokat, and Erzincan.
A.D. 1535	b	A/B	Reported near Erzincan.
A.D. 1481/82	d	B	Extensive destruction in Erzincan.
A.D. 1457	d	B	Reported 23 April. Extensive destruction in Erzincan.
A.D. 1374	d	B	Reported 8 December. The Erzincan city walls collapsed.
A.D. 1287	d	B	Reported 16 May. Extensive destruction in Erzincan.
A.D. 1254	a, d	E	Reported epicenter near Susehri, with damage also reported in Niksar and Erzincan.
A.D. 1236/37	d	A	Possibly doublet of 1206/7 AD earthquake. Caused collapse of a church in Erzincan.
A.D. 1206/7	d	A	Reported in Erzincan.
A.D. 1166	d	B	A strong earthquake reported in Erzincan. Possibly causing ~18k deaths.
A.D. 1050	a, d	A	Reported at Cankiri (~30km south of Ilgaz).
A.D. 1045	a, d	B	Erzincan was destroyed along with many churches in the region.
A.D. 1043	e	A/B	A rupture from Nicopolis (ancient city near modern Susehri) in a line to Erzerum is reported.
A.D. 1011	a, d	A	Reported earthquake in Erzincan. There was also a major flood in this year – the damage may be compounded reflecting a smaller earthquake.
3 rd , 5 th , 7 th Centuries A.D.	e	?	Vague reports of seismicity in Amasya, Niksar, and Nicopolis. Exact dates are not available.
A.D. 499	a, d	E/D	Reported in Niksar and Nicopolis.
A.D. 343	f	A/B	Almost total destruction of Niksar. The localized location of reports suggest this event may have been similar to the 1942 Earthquake on the northern side of the Niksar basin.
c.1200 B.C.	g	D?	A sequence of earthquakes along the NAF may be attributable to the destruction of a collection of major cities at the transition of the Bronze Age to the Iron Age.
References:			X – this column denotes our interpreted likelihood of rupture of the 1939 rupture segment of the NAF:
a: (<i>Ambraseys and Jackson</i> , 1998)			A: Probably did not rupture this segment
b: (<i>Ambraseys and Finkel</i> , 1995)			B: Possibly ruptured part of the segment
c: (<i>Sengor et al.</i> , 2005)			C: Possibly ruptured the whole segment
d: (<i>Guidoboni and Comastri</i> , 2005)			D: Probably ruptured part of the segment
e: (<i>Ambraseys</i> , 1970)			E: Probably ruptured the whole segment
f: (<i>Guidoboni et al.</i> , 1994)			
g: (<i>Nur and Cline</i> , 2000)			

1186 **Table 1.** Summary of historical earthquakes in the region of the 1939 Erzincan
1187 earthquake rupture segment.
1188

Sample #	Soil unit	Trench wall	CRA (years B.P.)	Calibrated Age years (A.D./B.C.) 2σ	
				unmodeled	modeled
<i>Trench T1</i>					
T1E1: younger than A.D. 1494					
37	C4	E	270 ± 35	A.D. 1494 – A.D. 1951	not modeled
<i>Trench T2</i>					
T2E0 and T2E1: younger than ~1660 A.D.					
42	Ps1a	W	160 ± 35	A.D. 1663 – A.D. 1953	not modeled
41	Ps1a	W	170 ± 35	A.D. 1657 – A.D. 1953	not modeled
40	Ps1b	W	31700 ± 150	29995 B.C. – 29559 B.C.	reworked
47	Ps1b	E	1370 ± 40	A.D. 608 – A.D. 761	reworked
50	S9	E	340 ± 35	A.D. 1468 – A.D. 1641	not modeled
T2E2: A.D. 200 - A.D. 1640					
43	Ps2a	W	1750 ± 50	A.D. 137 – A.D. 402	not modeled
49	Ps2b	W	1720 ± 40	A.D. 242 – A.D. 399	not modeled
<i>Trench T3</i>					
26	W2	W	710 ± 40	A.D. 1227 – A.D. 1388	reworked
T3E0 - base of W2 - interpreted to be the 1939 earthquake					
2	F1	E	60 ± 35	A.D. 1693 – modern	A.D. 1706 – A.D. 1926
B51	Ps2	E	150 ± 40	A.D. 1666 – A.D. 1953	A.D. 1666 – A.D. 1888
B53	F2	E	600 ± 35	A.D. 1297 – A.D. 1411	reworked
T3E1 - base of W3					
27	F3b	W	550 ± 35	A.D. 1311 – A.D. 1434	A.D. 1337 – A.D. 1440
B54	W4c	E	530 ± 35	A.D. 1317 – A.D. 1440	A.D. 1324 – A.D. 1428
6	W4c	E	570 ± 35	A.D. 1304 – A.D. 1425	A.D. 1305 – A.D. 1413
T3E2 - base of W4					
B55	F3a	E	790 ± 35	A.D. 1190 – A.D. 1281	A.D. 1189 – A.D. 1280
5	F3a	E	730 ± 35	A.D. 1222 – A.D. 1296	A.D. 1224 – A.D. 1291
B57	F3a	E	990 ± 35	A.D. 989 – A.D. 1154	A.D. 989 – A.D. 1153
28	F3/4u	W	3120 ± 30	1490 B.C. – 1314 B.C.	reworked
B60	W5b	E	1410 ± 40	A.D. 576 – A.D. 667	A.D. 578 – A.D. 669
T3E3 - base of W5					
B61	F4a	E	1770 ± 40	A.D. 136 – A.D. 381	A.D. 133 – A.D. 379
B64	F4b	E	2360 ± 40	A.D. 536 – 380 B.C.	reworked
25	F4b	W	3830 ± 40	2458 B.C. – 150 B.C.	reworked
24	F4b	W	2140 ± 40	353 B.C. – 55 B.C.	338 B.C. – 52 B.C.
23	F5	W	2150 ± 50	359 B.C. – 54 B.C.	363 B.C. – 122 B.C.
B68	F5	E	2600 ± 30	815 B.C. – 672 B.C.	811 B.C. – 568 B.C.
33	W6	W	1900 ± 30	A.D. 27 – A.D. 213	too young
T3E4 - base of W6					
12	F6c	E	4260 ± 30	2919 B.C. – 2779 B.C.	reworked
16	F6c	W	1820 ± 40	A.D. 86 – A.D. 323	too young
B70	F6c	E	2640 ± 40	890 B.C. – 774 B.C.	897 B.C. – 789 B.C.
10	F6c	E	4190 ± 30	2889 B.C. – 2676 B.C.	reworked
B71	F6c	E	3030 ± 30	1394 B.C. – 1213 B.C.	1359 B.C. – 1134 B.C.
17	F6c	W	3020 ± 40	1390 B.C. – 1130 B.C.	1347 B.C. – 1127 B.C.
34	F6b	W	1670 ± 40	A.D. 258 – A.D. 429	too young
B72	S4	E	3060 ± 40	1417 B.C. – 1220 B.C.	1381 B.C. – 1266 B.C.
T3E5 - base of W7					
B73	F7	E	3290 ± 30	1628 B.C. – 1500 B.C.	reworked
9	F8	E	1600 ± 40	A.D. 385 – A.D. 553	too young
B81	F9	E	3070 ± 30	1413 B.C. – 1268 B.C.	1420 B.C. – 1321 B.C.

1190 **Table 2.** Summary of sample radiocarbon ages from this study. CRA is Conventional Radiocarbon Age
1191 (*Stuiver and Polach, 1977*). A table with more extensive data is presented in Table A.B-1 (Annex B).
1192 Figure 9 is a graphical presentation of the order-constrained Bayesian model (electronic supplement 1)
1193 compiled using selected samples from trench T3.
1194

1195

Variable	2σ Age Range (years)
IET0-1	135–530
IET1-2	75–504
IET2-3	654–1086
IET3-4	993–1450
IET4-5	460–701
SIET	109–1385 (bimodal)
RIavg	646–669

1196 **Table 3.** Duration between earthquakes derived from the OxCal model (see Fig. 9 and
1197 electronic supplement 1). Note: IET0-1 is the inter-event time between event 0 and event
1198 1. SIET is summed inter-event time, RIavg is the average recurrence interval.
1199

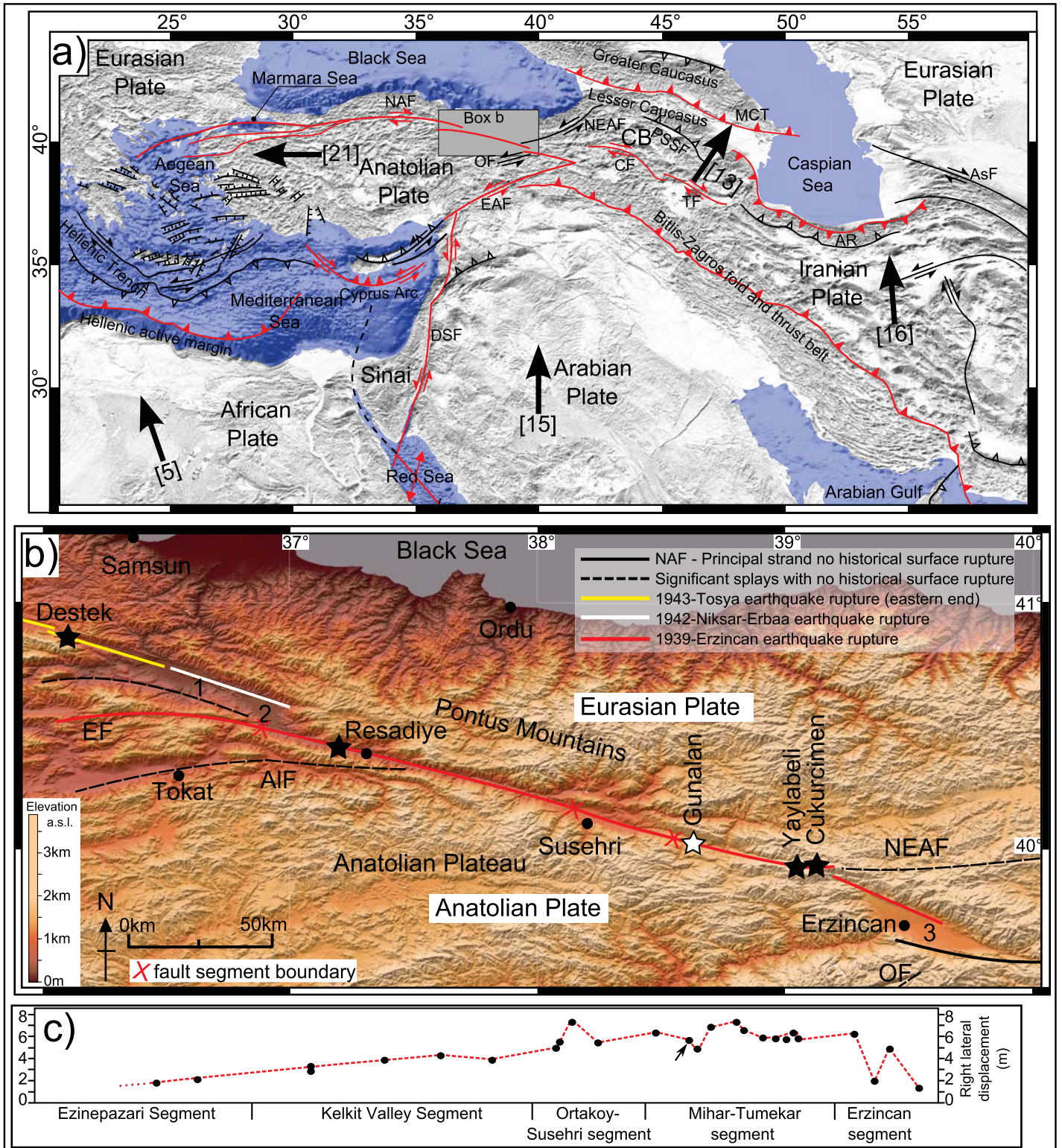
Resadiye (Fraser, 2009b)	Gunalan (this study)	Yaylabeli (Kozaci et al., 2011)	Cukurcimen (Hartleb et al., 2006)	Historical Earthquakes (See Table 4)
Event 0 unconstrained	E0 unconstrained	E1 A.D. 1150–A.D. 1939	Event A unconstrained	A.D. 1939 Erzincan earthquake
Event 1 A.D. 1570–A.D. 1939	E1 A.D. 1408–A.D. 1804	—	—	A.D. 1668 ?
—	E2 A.D. 1259–A.D. 1391	E2 A.D. 1150–A.D. 1939	Event B A.D. 980–A.D. 1420	A.D. 1254
—	—	E3 A.D. 910–A.D. 1110	Event C A.D. 930–A.D. 1070	A.D. 1045
—	—	E4 A.D. 710–A.D. 850	—	—
Event 2 A.D. 262– A.D. 642	E3 A.D. 241– A.D. 644	E5 A.D. 320– A.D. 690	Event D A.D. 360–A.D. 540	A.D. 499
Event 3 258 B.C.– A.D. 206	—	X	Event E 230 B.C.–A.D. 50	—
Event 4 908 B.C.–702 B.C.	E4 881 B.C.–673 B.C.	X	Possibly Event F 1450 B.C.–800 B.C.	—
—	E5 1406 B.C.–1291 B.C.	X	Possibly Event F 1450 B.C.–800 B.C.	1200 B.C.
Event 5 2020 B.C.–1804 B.C.	X	X	X	—
Event 6 2280 B.C.–2066 B.C.	X	X	X	—

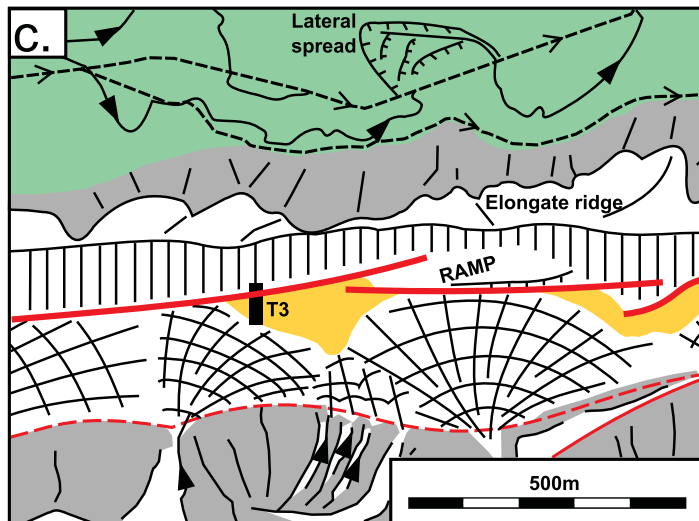
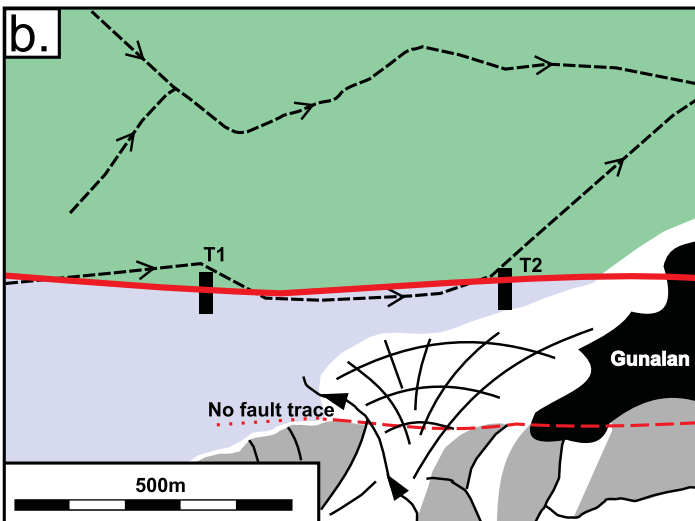
— Earthquake not recognized
X Older than exposed earthquake record

1201 **Table 4.** Earthquake timing comparison with nearby paleoseismic studies on the North
1202 Anatolian Fault and correlated historical earthquakes (historical-earthquake records are
1203 summarized in Table 1), summarized graphically in Figure 10. Note: ‘—’ corresponds to
1204 ‘earthquake not recognised’ and ‘X’ corresponds to ‘older than exposed in earthquake
1205 record’.
1206

Event	Event Number (in this study)	Segments ruptured ^a	Total length of rupture (km)	Magnitude estimate (Mw) ^b	
				Maximum	Minimum
<i>Individual fault segments</i>					
schematic	-	A	90	7.1	7.6
schematic	-	B	100	7.1	7.7
schematic	-	C	45	6.7	7.3
schematic	-	D	65	6.9	7.5
schematic	-	E	60	6.9	7.4
<i>Scenarios</i>					
A.D. 1939	E0	A, B, C, D, E	350	7.7	8.3
A.D. 1668	E1	A, B, C, D,	250	7.6	8.3
A.D. 1254	E2	D, E	170	7.2	7.8
A.D. 1045	Not observed	D (partial) , E	100	7.1	7.7
A.D. 499	E3	A, B, C, D, E	360	7.7	8.4
250 B.C. - A.D. 100	Not observed	unsure			
900 B.C. - 700 B.C.	E4	A, B, C, D, E	360	7.7	8.4
~1200 B.C.	E5	D, E (?)	170	7.2	7.8

1208 **Table 5.** Earthquake magnitude estimates for a range of rupture lengths. Note^a letters
1209 correspond to fault segments shown on Figure 1: A- Ezinepazari, B- Kelkit Valley, C-
1210 Ortakoy - Susehri, D- Mihar - Tumekekar, E- Erzincan. Note^b, magnitude estimated
1211 using formula and regression coefficients from *Wells and Coppersmith et al.* (1994),
1212 see text for description.





Legend

- Inter-fan wetland
- Alluvial flood plain - dry
- Alluvial flood plain - damp
- Hilly terrain. Ridges are shown with black lines and crude shading of ~northwest facing slopes is shown with grey.

- Stream
- Canal
- Master fault
- Fault (did not rupture in 1939)
- Scarp (teeth show ~height)
- Alluvial fan

- T1 Trench location
- Photo taken from apex looking toward the fading direction.
- 5 Approximate location of displacements associated with the 1939 earthquake according to Kocyigit 1990. Number refers to that used in text.

